Department of Physics and Astronomy

University of Heidelberg

Diploma Thesis

in Physics
submitted by

Mustapha Al Helwi

born in Beirut, Lebanon

2010

Gain Calibration of the ALICE Transition Radiation Detector with Krypton-83

This diploma thesis has been carried out by Mustapha Al Helwi at the Physikalisches Institut at the University of Heidelberg under the supervision of Helmholtz Young Investigator Dr. Kai Schweda

Gain Calibration of the ALICE Transition Radiation Detector with Krypton-83m

The ALICE Transition-Radiation Detector (TRD) at the LHC is designed for electron identification, charged particle tracking and providing a fast trigger. The TRD consists of 18 super-modules with 540 readout drift chambers filled with Xe/CO_2 gas. In order to guarantee a high quality of the collected data a uniform gain is essential. The gain contains both gas and electronics response which may vary throughout the detector.
Within this diploma thesis a gain calibration was performed for the first time for a Transition Radiation Detector with Krypton (^{m83}Kr) as an electron source. Seven super-modules were installed in the ALICE setup with the full data readout chain and participated in the Krypton calibration data taking. Gain corrections for these were determined at the finest detector granularity, i.e. pad by pad.
An analysis algorithm that analyse the Krypton data and determine the gain parameters both on chamber and pad level was developed. The gain parameters are added to the detector data base in a defined format to be used for offline tracking and to be uploaded to the detector readout front-end-electronics.

Kalibration der Verstärkung des Übergangsstrahlungsdetektors von ALICE mit Krypton-83m

Der Übergangsstrahlungsdetektor (TRD) für ALICE am LHC identifiziert Elektronen, erweitert die Spurrekonstruktion geladener Teilchen und stellt ein schnelles Trigger-Signal zu Verfügung. Der TRD besteht aus 18 Supermodulen mit insgesamt 540 Auslese-Driftkammern, die mit Xe/CO_2 Gas gefüllt sind. Zur Gewährleistung einer hohen Qualität der erhobenen Daten ist eine gleichmäßige Verstärkung von wesentlicher Bedeutung. Diese Verstärkung beinhaltet sowohl die Gas- und Elektronik-Verstärkung, die innerhalb des Detektors variieren kann.
Im Rahmen dieser Diplomarbeit wurde die Kalibrierung der Verstärkung zum ersten Mal für einen Übergangsstrahlungsdetektor mit Krypton (^{m83}Kr) als Quelle für Elektronen im dynamischen Bereich des TRD durchgeführt und ausgewertet. Zum Zeitpunkt der Durchführung der Kalibrierungsmessung waren sieben Supermodule mit deren vollständigen Auslese-Elektronik installiert. Korrekturfaktoren der Vertärkung wurden für diese für jedes Pad einzeln ermittelt, was der feinsten Granularität des Detektors entspricht.
Für die Gesamtauswertung wurde ein Analyse-Algorithmus entwickelt, das die Kryptondaten auswertet und die Verstärkungsparameter sowohl auf Kammer- als auch auf Pad-Ebene bestimmt. Sämtliche Verstärkungsparameter stehen nun in einem definierten Format in der Detektor-Datenbank zur Verfügung zur Verwendung in der Offline-Spurrekonstruktion als auch zum Hochladen in die front-end Detektorausleseelekronik.

Contents

1. Introduction

On 23rd of November 2009, the Large Hadron Collider (LHC) restarted its operation at the European Organization for Nuclear Research CERN near Geneva, Switzerland. Collisions of protons as well as collisions of lead-ions will be part of the LHC program for the next years. Hereby the LHC will help physicists to answer many of the fundamental questions, i.e. the Higgs mechanism, the quark-gluon plasma, supersymmetry, etc.
The Quark-Gluon Plasma (QGP), a state of matter which have existed shortly after the Big Bang is one of the LHC main outstanding questions. The QGP was searched for at the Bevalac at the Lawrence Berkeley National Laboratory (LBNL), the Alternating Gradient Synchrotron (AGS) at the Brookhaven National Laboratory (BNL) , Super Proton Synchrotron (SPS) at CERN in Geneva and Relativistic Heavy Ion Collider (RHIC) at BNL. A brief history of the Heavy-Ion physics is shown in table 1.1.
The Large Hadron Collider (LHC) will provide collisions at particle energies that

Start	Accelerator	Laboratory	Projectile	Energy $\sqrt{s_{NN}}$
1974	Bevalac	LBNL	O, Ne	$1-2$GeV
1985	AGS	BNL	Si	≈ 5GeV
1985	SPS	CERN	O, S	≈ 20GeV
1994	SPS	CERN	Pb	17GeV
2000	RHIC	BNL	Au	200GeV
2010	LHC	CERN	Pb	5500GeV

Table 1.1.: Overview of accelerators of heavy-ion physics.

have never been reached before, i.e. it will allow insight into energy regions beyond SPS and RHIC. A Large Ion Collider Experiment (ALICE) is one of six experiments at the LHC and it is especially designed for heavy-ion collisions. ALICE was designed and constructed for investigations of lead-lead collisions and thus for the characterization of the QGP.
The main tracking devices of ALICE experiment are the Inner Tracking System (ITS), the Time Projection Chamber (TPC) and the Transition Radiation Detector (TRD). The main purposes of the TRD are the improved separation of electrons and

pions, the reconstruction of tracks of charged particles and providing fast trigger capabilities. The physical observables that benefit from the TRD Trigger are among other the J/ψ production, Υ production and Jet production with Jet energies up to 100 GeV.
The cylindrical detector structure consists of eighteen sectors, the so called super modules, with a total of 540 readout drift chambers. One TRD chamber consists of a radiator part and a multiwire proportional chamber filled with Xe/CO_2. A particle traversing the TRD create a transition radiation when it passes the radiator depending on its Lorentz factor and ionize the gas along its path in the drift region. The ionized electrons drifts in a uniform electrical field toward the amplification region and induce a signal after beeing amplified. The readout electronics amplifies and digitizes the signal.
For particle identification, only reconstruction of tracks is not sufficient. Information about the energy deposition per unit of length dE/dx of charged particles within the drift chamber is also needed.
This energy is proportional to the charge induced by the electron cloud on the pads. Since the individual electronic-channels have different amplification factors, and the gas amplification might varie locally, e.g. by inhomogeneity of the electric field, the measured charge has to be corrected accordingly.
Within this thesis the gain parameters for the ALICE Transition Radiation Detector have been extracted from a dedicated calibration run with a Krypton source. The radioactive ^{m83}Kr, which was homogeneously distributed in the TRD volume by the gas circulation system, releases electrons with energies between 9 keV and 42 keV. In total $2.8 \cdot 10^9$ Krypton decays in 181 runs were recorded and analyzed. The known energy deposition from electrons resulting from the decay of the metastable Krypton ($^{m83}\text{Kr} \longrightarrow e- + {}^{83}\text{Kr}$) allows the gain calibration of the gas and electronics amplification.
This thesis is organized as follows.
Chapter 2 gives an introduction to the ALICE experiment relevant theoretical basics of high energy physics. The Large Hadron Collider and the ALICE experiment are discussed in chapter 3. The Transition Radiation Detector (TRD) is described in chapter 4. In chapter 5 and 6 the concept of the Krypton calibration and its experimental setup are introduced. Chapter 7 presents the analysis strategy and results of the gain calibration. The gain dependence on the applied anode voltage is discussed in chapter 8 and results are compared to previous studies. A summary is given in chapter 9.

Figure 1.1.: ALICE event display image of proton-proton collision at 7 TeV (run nr.114783, event nr.126). Left: Three dimensional view, top right: beam view, top left: side view [1].

2. Theoretical Background

2.1. Basic Constituents of Matter

Already 400 B.C. it was assumed that all matter is made-up from basic constituents. When searching for these basic constituents of matter, smaller and smaller particles were found which appear to be divisible as well: In the 19^{th} century it was discovered that all matter consists of atoms [14]. About 100 elements were known, organized by their properties into a limited amount of groups, described by the periodic table. This gave a hint that atoms have an inner structure. With the discovery of the electron and of radioactivity, a new way for the investigation of matter was found. In the early 20^{th} century, a scattering experiment of helium nuclei in a gold foil showed that the atom consists of a small nucleus with a cloud of electrons surrounding it. But the nucleus is also divisible: After the discovery of the neutron, the nucleus was found to be composed of protons and neutrons, the so-called nucleons. In 1930, a new particle, the neutrino, was postulated to describe the β-decay of nuclei. Altogether four particles were then known which could account for most observed phenomena of atoms and nuclei at that time: the proton, the neutron, the electron, and the neutrino. In the 1950s and 1960s, accelerator experiments discovered that protons and neutrons are one of the most frequent representatives of many existing particles, the so called hadrons. Due to measured properties of some hadrons, an inner structure was postulated, including smaller constituents, the so-called quarks. The standard model provided an answer about the composition of the hadrons. In the model, all hadrons consist of two or three quarks, which divides the hadrons respectively in mesons and baryons [15].

2.2. The Standard Model

In the standard model two kinds of particles, the quarks and the leptons, are the constituents of all matter, and four different forces describe the interaction between these particles. Within the model they are indivisible, point-like particles. The quarks and the leptons can be classifed into three so-called generations, each containing two different particles.
The six different quarks are called up, down, strange, charm, top, and bottom

quark. They carry a color charge, named red, blue, or green, which is related to their strong interaction, and an electric charge of $\frac{-1}{3}e$ or $\frac{2}{3}e$. The group of leptons is divided into the electron, the muon and tauon with an electric charge of $-e$, and the related neutral neutrinos ν_e , ν_μ, and ν_τ . Each of these twelve particles also has an anti-particle. Altogether 24 particles are nowadays seen as the basic constituents of matter. The four existing and known fundamental forces are the gravitation, the weak and the strong nuclear forces, and the electro-magnetic force. Each force is mediated by its force carriers. The force carriers of the Standard Model are gauge bosons. The standard model of particle physics describes the weak and strong nuclear force and the electro-magnetic force, but not the gravitation. Fundamental particles, the interaction forces and their gauge bosons are shown in Fig. 2.1.

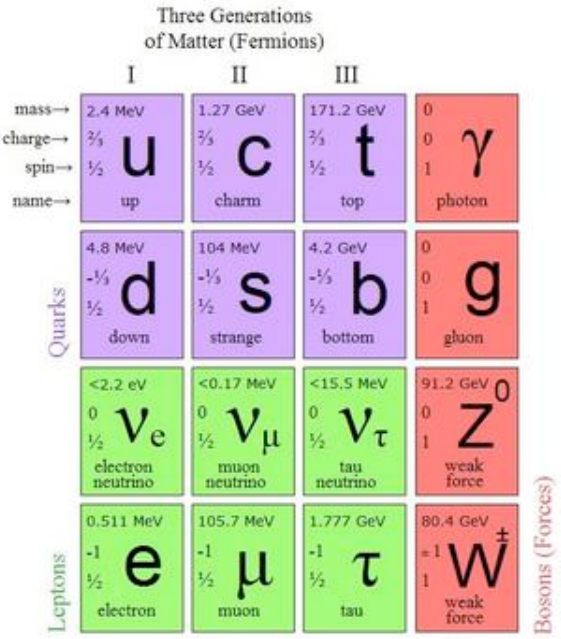

Figure 2.1.: The Standard Model of elementary particles, with the gauge bosons (force carries) in the rightmost column [16].

2.3. The Quark-Gluon Plasma (QGP)

The interaction between quarks is strong at large distances and weakens at smaller ones. These two phenomena are called confinement and asymptotic freedom. At low temperatures and low densities, the strongly interacting partons, quarks and gluons, are confined in a small space region within the hadrons. When the temperature and/or the density of nuclear matter becomes very high, the partons transform into

a deconfined phase of matter, called quark-gluon plasma (QGP).
The phase diagram of nuclear matter is shown in figure 2.2. The axes are the temperature T and the net baryon density ρ. ρ is defined as the number of baryons minus the number of anti-baryons per volume unit.
According to quantum chromodynamics, the theory of the strong force, a phase transition from hadronic to partonic [1] matter should occur at a critical temperature T_c and energy density ϵ_c . The confined partons become quasi-free. For $\mu_B = 0$, the transition temperature from nuclear to partonic matter can be estimated as $\sim 170MeV$ [17].
The solid lines in fig. 2.2 indicate first-order phase transitions, while the dashed line indicates a possible region of a continuous but rapid, so-called crossover, phase transition. The circle in between gives the second-order critical endpoint of a line of first-order transitions. The experiments at LHC are predicted to generate a high-temperature, low-density QGP, which will freeze out on the crossover phase transition.

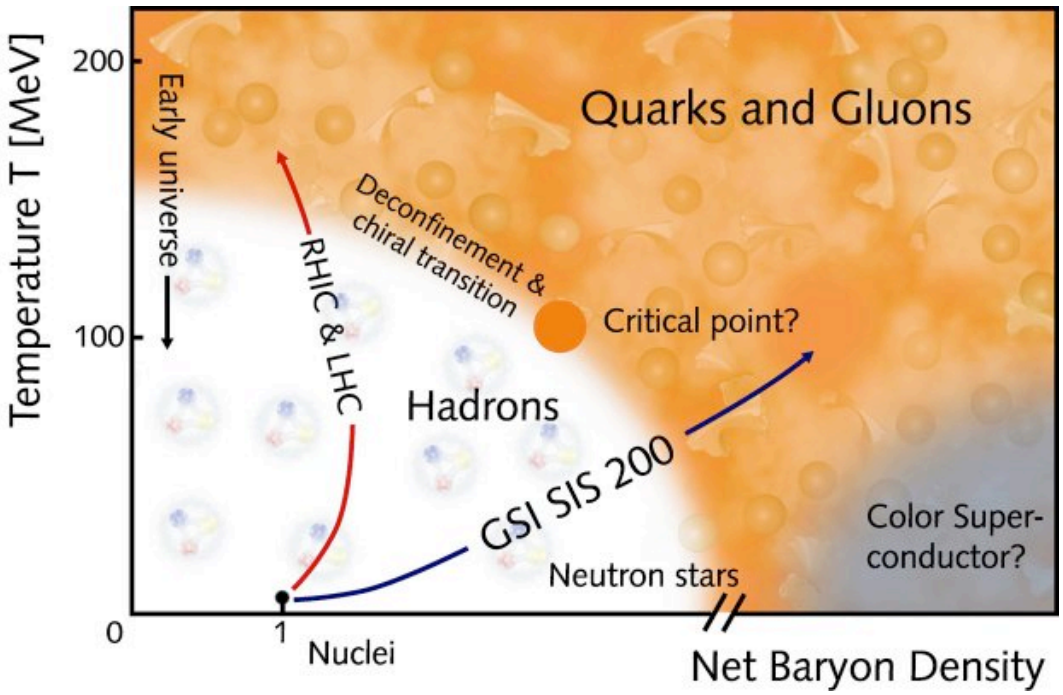

Figure 2.2.: A schematic phase diagram of nuclear matter. The net baryon density is the density of baryons minus the density of antibaryons [18].

[1] In particle physics, the parton model was proposed by Richard Feynman in 1969 as a way to analyze high-energy hadron collisions [19]. It was later recognized that partons describe the same objects now more commonly referred to as quarks and gluons.

2.4. Generating the QGP in Heavy-Ion Collisions

According to the theories, shortly after the big bang quarks and gluons were deconfined in the quark gluon plasma. While the universe expanded and cooled down, the partons combined to hadronic matter. Today the average temperature and density in the universe are much lower. One opportunity to study the QGP with its properties is to produce such a state of matter in heavy-ion collisions at accelerator facilities. In these collisions, a shortly living fireball is produced, in which high densities and temperatures can be reached. In order to interpret the generated system and its behavior as the QGP, the system under consideration should consist of a large number of particles, such that the medium in the fireball reaches an equilibrium state.
So collisions can give evidence on the properties of nuclear matter, explain the phase diagram of nuclear matter, and also give hints on the evolution of the universe. In Fig. 2.3, a simulated collision between two nuclei is shown, divided into four steps of time evolution:

(a) the Lorentz contracted nuclei flying towards each other,

(b) the partons collide and the nuclei penetrate each other.

(c) The QGP can be generated in the region between the diverging fractions of the nuclei.

(d) The partons freeze out and combine to hadrons. Overall a huge amount of hadrons, leptons, and photons is emitted in the collision.

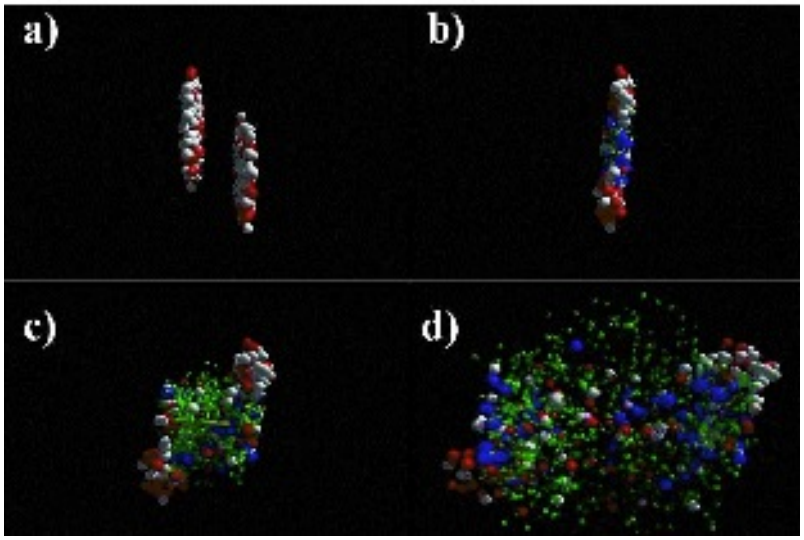

Figure 2.3.: Simulation of the time evolution of a collision between two heavy nuclei. Due to the Lorentz contraction the two nuclei appear as two thin discs in the laboratory frame.

3. LHC and ALICE

3.1. The Large Hadron Collider

The Large Hadron Collider (LHC) is located at the European Organisation for Nuclear Research (Conseil Européen pour la Recherche Nucléaire, CERN) near Geneva, Switzerland. The first circulating beam was seen on the 10^{th} of September 2008. An incident occurred nine days later which damaged a couple segments of the collider. After about one year of repairing the damage, the first collisions took place on the 23^{rd} of November 2010. The LHC has become then on the 30^{th} of November 2009 the world's highest energy particle accelerator, having accelerated its twin beams of protons to an energy of 1.18 TeV. This exceeds the previous world record of 0.98 TeV, which had been held by the US Fermi National Accelerator Laboratory's Tevatron collider since 2001. At the LHC two counter rotating beams of protons or heavy ions are brought to collision at an unprecedented high center of mass energy of up to $\sqrt{s} = 14$ TeV in p+p collisions at a luminosity of $\mathcal{L} = 10^{34}\ cm^{-2}s^{-1}$ [24]. Due to this enormous collision energies new insights into the structure of matter and fundamental forces will be possible. In lead-lead collisions the center of mass energy of up to $\sqrt{s} = 5.5$ TeV per nucleon-nucleon pair which will be reached is higher by a factor of 30 compared to the collision energies of the Relativistic Heavy Ion Collider (RHIC) at the Brookhaven National Laboratory (BNL). The designed nominal luminosity in lead-lead collisions in LHC is $\mathcal{L} \approx 10^{27}\ cm^{-2}s^{-1}$.
The LHC was constructed inside the existing tunnel of the Large Electron Positron (LEP) collider which stopped its operation in 2000. A schematic overview of the CERN accelerator system is shown in fig. 3.1 and discussed in details in the following paragraph.

Protons from a 90 kV duoplasmatron proton-source are accelerated in the linear accelerator LINAC2 to a kinetic energy of 50 MeV and then passed on to the multi ring Proton Synchrotron Booster (PSB) where they are accelerated to 1.4 GeV. In the Proton Synchrotron (PS) they reach 26 GeV and their bunch patterns are generated. After the transfer to the Super Proton Synchrotron (SPS) protons are accelerated to 450 GeV and injected into the LHC ring with about 27 km circumference where they reach 7 TeV. To keep the protons along the ring, 1232 superconducting dipole magnets are installed. They are cooled down to 1.9 K by liquid helium and provide a magnetic field of up to 8.3 T. Additionally, 392 quadrupole magnets keep the beams

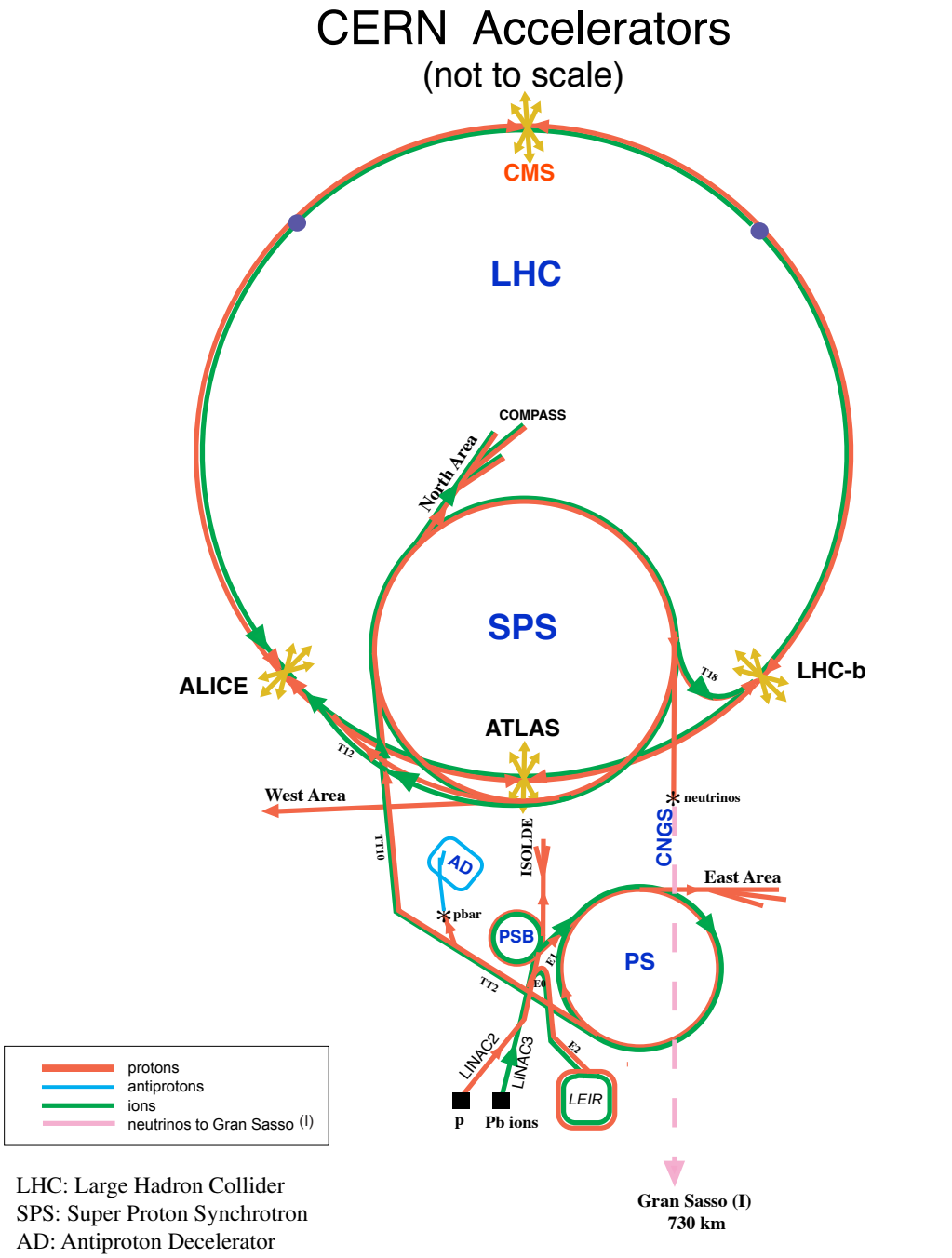

Figure 3.1.: Overview of the accelerator system at CERN [1].

focused.
Lead ions from an electron cyclotron resonance source are bunched and accelerated by a radio frequency quadrupole. They are selected in the charge state Pb^{27+} and further accelerated in the linear accelerator LINAC3 to 4.2 MeV/nucleon. After that, they are stripped by a carbon foil and the charge state Pb^{54+} is selected in a filter line. These selected ions are further accelerated in the low energy ion ring (LEIR) to an energy of 72 MeV/nucleon. From there the ions are transferred to the PS where they are accelerated to 5.9 GeV/nucleon and sent to the SPS. In between they pass another foil which fully strips the ions to Pb^{82+}. The SPS accelerates the fully stripped ions to 177 GeV/nucleon, before injecting them into the LHC where they reach a maximum energy of 2.76 TeV/nucleon.
The two beams are brought to collision at eight interaction points. At four of the interaction points the main experiments are located as indicated in fig. 3.2.

ATLAS: The main goal of A Toroidal LHC Apparatus (ATLAS) experiment is the discovery of the Higgs-Boson and the investigation of theories beyond the standard model, i.e. the search for supersymmetric particles and extra dimensions.

CMS: The Compact Muon Solenoid (CMS) is designed to analyze the nature of matter. The CMS and the ATLAS experiments are built for the same purpose applying complement detector technologies.

LHCb: The LHC Beauty (LHCb) experiment is built to observe CP violation in B-meson systems. The results are dedicated to understand the difference between matter and antimatter in the universe.

ALICE: A Large Ion Collider Experiment (ALICE) is the dedicated heavy ion detector at the LHC. The ALICE detector is designed to identify and characterize the quark gluon plasma. ALICE is briefly described in the next section.

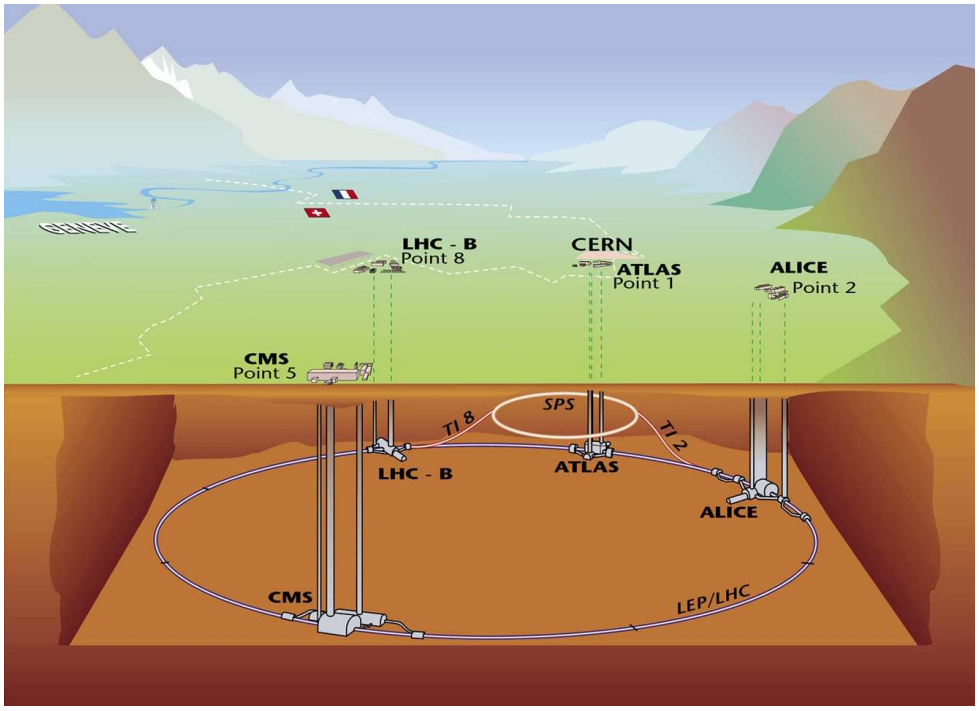

Figure 3.2.: Schematic view of the Large Hadron Collider and its four experiments ALICE, ATLAS, LHCb and CMS [1].

3.2. A Large Ion Collider Experiment

A Large Ion Collider Experiment (ALICE) is designed to determine the identity and precise trajectory of more than ten thousand charged particles over a large transverse momentum range from 100 MeV/c to 100 GeV/c. The layout of the ALICE detector which is split into the so-called Central Barrel and the Muon arm is illustrated in Fig. 3.3.
The Muon Arm covering a pseudo-rapidity range from $-2.4 < \eta < -4.0$ is dedicated to the measurement of muons. Hadrons and electrons are removed by the absorber made predominantly out of carbon and concrete. The muon tracks are bent for momentum measurement by the dipole magnet with an integrated field of 3 Tm and then detected by the tracking system which covers a total area of about 100 m^2 and achieves a spatial resolution of about 100 μm. The tracking system consists of cathode pad chambers which are arranged in five stations: two are placed before, one inside and two after the dipole magnet. The stations are made of two chamber planes. Their size ranges from a few square metres for the first station to more than 30 m^2 for last station. The ALICE central barrel covers the kinematic region around pseudo-rapidity $|\eta| < 0.9$ and is surrounded by the L3 solenoidal magnet which produces a homogeneous magnetic field of up to 0.5 Tesla parallel to the beam axis. This magnetic field provides momentum dispersion for charged particles in the plane transverse to the beam axis.

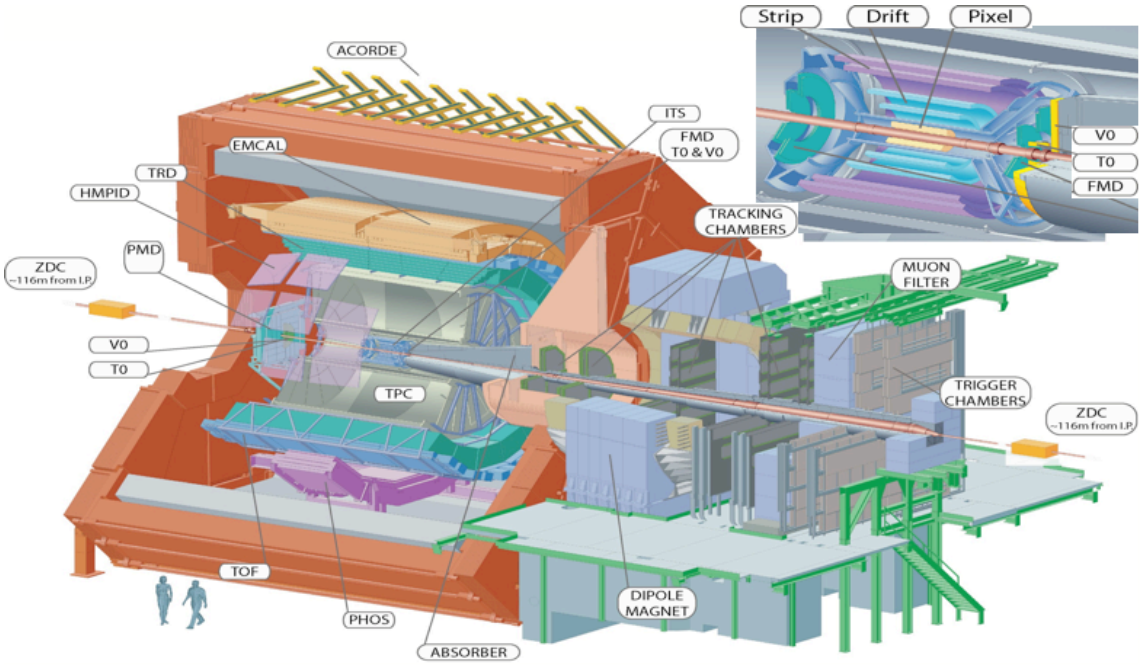

Figure 3.3.: Schematic layout of the ALICE detector. [25].

The central part of ALICE is an assembly of various detectors. The detectors providing information like momentum, vertex coordinates and particle identification are the Inner Tracking System (ITS), the Time Projection Chamber (TPC), the Transition Radiation Detector (TRD) and the Time of Flight detector (TOF).

Inner Tracking System
The main purpose of the Inner Tracking System (ITS) is the determination of vertices with high spatial resolution. Additionally the ITS provides tracking and identification of particles with momenta down to 100 MeV/c and improves the momentum resolution of tracks with higher momentum. To cope with the large number of charged particles expected to be produced in a lead-lead collision the ITS has a high granularity and radiation hardness. To keep the distortion of tracks of charged particles to a minimum, the total thickness of ITS was optimised to be 7% radiation length. Therefore the ITS consists of six cylindric layers each of a different type: the first two layers are Silicon Pixel Detectors (SPD), followed by two layers of Silicon Drift Detectors (SDD) and two layers of double-sided Silicon micro-Strip Detectors (SSD). These six layers are located at radii $r = 4, 7, 15, 24, 39$ and 44 cm [25]. The first layer is located only 4 cm away from the beam axis, and covers almost four units of pseudo-rapidity. The two layers of SPD have a spatial resolution of 12 μm in the $r\phi$-plane and 70 μm in z-direction, the resolution of the two layers of SDD is 28 μm in z-direction and 38 μm in $r\phi$-direction while the two outer layers have a 20 μm $r\phi$-resolution and 830 μm z-resolution. The precise measurement in ITS allows the extrapolation of tracks back to the primary vertex of the collision with an impact parameter resolution better than 100 μm [26].

Time Projection Chamber
The Time Projection Chamber (TPC) is the main tracking detector in the central barrel ($|\eta| < 0.9$) of the ALICE experiment. The TPC provides charged particle momentum measurement and primary vertex determination with precise momentum resolution at a large tracking efficiency of 90% and two-track separation up to a p_T region of more than 10 GeV/c. Additionally correct pattern recognition of the high multiplicity Pb+Pb central collisions at the LHC energy are achieved by the TPC. Up to 20 thousand primary and secondary charged tracks per event are expected in the sensitive volume. The cylindric TPC has an inner radius of 80 cm, an outer radius of 250 cm and an overall length of 5 m, covering full azimuth. This means the ALICE TPC is with its active volume of about 95 m^3 the largest TPC ever built. The total material budget is kept at the level of 3% radiation length to ensure minimal multiple scattering and secondary particle production. The TPC cylindrical field cage of 88 m^3 size is divided by a central electrode into two drift regions. The high voltage central electrode provides a uniform electrostatic field of 400 V/cm. The whole drift volume in the cage is filled with a gas mixture of 85% Ne / 10% CO_2/ 5% N. Within this drift gas the maximum drift

time is $t \sim 88\ \mu s$. Three-dimensional space points are reconstructed from the measured drift time (z-direction) and the position on the cathode pads (x, y-direction) of the induced signal. In total, the TPC provides up to 160 space points for each particle trajectory. Additionally the TPC contributes strongly to the particle identification. Particles are identified within the TPC by their specific loss of energy due to interactions with the TPC gas. More details are discussed in the next chapter.

Transition Radiation Detector
The Transition Radiation Detector (TRD) consists of 18 supermodules with 540 readout drift chambers filled with Xe/CO_2 gas. It identifies electrons with $p_T > 1$ GeV/c and provides fast trigger capabilities within 6 μs. More details of the TRD are described in Chap. 4.

Time Of Flight
The Time Of Flight (TOF) detector is the most outer part of the ALICE tracking chain and extends the identification of hadrons, namely π, K, p, in a momentum range up to 4 GeV/c by measuring the time a particle needs to fly from the interaction point to a radial distance of approximately 4 m. TOF is composed of 18 supermodules surrounding the 18 TRD supermodules and covers a surface larger than 160 m^2. The TOF detector is composed of multigap resistive plate chambers (MRPC) which achieve a time resolution of 65 ps at a rate of more than 50 Hz/cm^2 [1].

The detectors dedicated to a specific physics task are the Photon Spectrometer (PHOS) measuring high momentum photons, the High Momentum Particle Identification (HMPID) to separate kaons from pions and protons and the Electro-magnetic Calorimeter (EMCAL) for the detection of high momentum electro-magnetic probes. These three detectors cover only a small part of the full acceptance. A detailed description of the individual subcomponents of ALICE is found in [27].

ALICE Coordinate System
The *global* coordinate system is defined in accordance with the LHC [25]. The origin is defined as the arbitrary center of the detector where the collision ideally occurs. The z-axis is parallel to the beam direction. Perpendicular to the z-axis is the transverse $r\phi$-plane in x, y-direction, where the x-axis is horizontal, and the y-axis is vertical. The system is right-handed, with positive x pointing inwards referred to the LHC ring, positive y pointing upwards and positive z pointing in the opposite direction of the muon arm. The azimuthal angle Φ increases, starting in x-direction $\Phi = 0°$ counter-clockwise viewed from the z-direction. This coordinate system is generally used to locate an object described in the global view of the detector, e.g. the sub-detectors, the track vertex, etc.
Clusters and tracks are always expressed in a *local* coordinate system related to

a given sub-detector, e.g. TPC module, ITS module, etc. This local coordinate system is defined as following:

- it is a right-handed Cartesian coordinate system;
- its origin and the z axis coincide with those of the global ALICE coordinate system;
- the x axis is perpendicular to the sub-detector's sensitive plane e.g. the TRD pad plane.

This choice reflects the symmetry of the ALICE setup and therefore simplifies the reconstruction equations. It also enables the fastest possible transformations from a *local* coordinate system to the global one and back again, since these transformations become single rotations around the z-axis.

4. The Transition Radiation Detector

4.1. Energy Loss of Charged Particles

A charged particle deposits energy if it traverses matter, e.g. if it passes through the drift chambers gas of the TRD. Processes of energy loss by ionisation are described by the *Bethe-Bloch formular* [15]. Radiative energy loss or *Bremsstrahlung* and transition radiation are further processes of energy loss. These processes depend on the particle velocity. Thus, at a given momentum it allows for the determination of the particle mass and hence its identity.

Ionisation and the Bethe-Bloch Formula

When passing through a medium a charged particle loses energy via ionisation or excitation of the constituent atoms. The mean energy loss per path length is derived from the Rutherford formula for elastic scattering and is described by the *Bethe-Bloch formula* [28]:

$$-\frac{dE}{dx} = \frac{4\pi N_A z^2 e^4}{mv^2}\frac{Z}{A}\left[\ln\left(\frac{2mv^2}{I(1-\beta^2)}\right) - \beta^2\right] \tag{4.1}$$

The path length x in the medium is usually given in [$g\ cm^{-2}$ or $kg\ m^{-2}$] and corresponds to the amount of matter traversed. Here, m is the electron mass, z and v are the charge and velocity of the traversing particle. The relativistic velocity is given by $\beta = v/c$, N_A is Avogadro's number and I is an effective ionisation potential of the atom species of the medium, averaged over all electrons, with approximate magnitude $I = 10\ Z\ eV$ [28]. Z and A are the atomic number and mass number of the medium atoms. The energy loss described by Eq. (4.1) drops with $1/\beta^2$ for small $\gamma = E/Mc^2 = (1-\beta^2)^{-1/2}$, M being the mass of the passing particle, reaches a minimum for $E \simeq 3\ Mc^2$ and increases afterwards logarithmically with γ. The drop is due to the particle having less time to interact with the medium the faster it gets. The slow rise for high γ originates from relativistic effects, leading to an increase of the transverse electric field of the particle which enables atoms of the medium that are further away from the particle's path to interact with the particle.

This effect saturates into the Fermi plateau, since the polarisation of the medium shields the electro-magnetic field of the moving particle.
The energy loss described by Eq. (4.1) is independent of the particle mass M. The specific energy loss of different particles with the same momentum $p = Mv$ is used to identify the particle species if momentum of the particle is known, e.g. via the curvature of the path in the magnetic field.

Bremsstrahlung

Additionally to ionisation, particles loose energy due to radiation of photons when traversing matter. The electric field of the atomic nuclei of the medium decelerates the passing particle, resulting in the emission of a photon, therefore the name *Bremsstrahlung*.
The average energy loss per unit length is given by:

$$-\frac{dE}{dx} = 4\alpha_e N_A \frac{Z^2}{A} z^2 r_0^2 E \ln \frac{183}{Z^{1/3}} \tag{4.2}$$

$$-\frac{dE}{dx} = \frac{E}{X_0} \tag{4.3}$$

With variables and constants as in Eq. (4.1) and the classical electron radius $r_0 = \hbar/c\alpha_e M$, where M is the electron mass. Energy loss from Bremsstrahlung drops with the traversing particle mass squared M^{-2} and rises proportional to its energy E. Therefore Bremsstrahlung is mainly seen from electrons. X_0 is the characteristic radiation length after which the energy of the particle is reduced by a factor $1/e \approx 1/3$.
For low energies the energy loss is dominated by ionisation. However the ionisation effect is almost constant for high energies, while the radiative energy loss rises with E Bremsstrahlung becomes the dominating effect. For electrons the critical energy at which both effects contribute equally is:

$$E_c \simeq \frac{600}{Z}\ MeV. \tag{4.4}$$

Transition Radiation

Another radiative effect is transition radiation (TR). It is produced if an ultra-relativistic particle crosses the boundary surface of two media with different dielectric constants, fraction indices n, respectively. The electro-magnetic field of a charged particle changes with the dielectric constant of the medium by which it is surrounded. Since the electric field is continuos at the boundary region the field of

the charged particle has to change, hence radiation is emitted. A qualitative description of transition radiation is obtained from classical electrodynamics by using the model of a mirror charge of the particle within the medium with opposite charge and equal distance to the boundary surface. The actual particle and its mirror self form a dipole evolving in time since the particle is moving towards the boundary and so is its mirror charge. Therefore radiation is emitted in an angle of $\Theta \propto 1/\gamma$. The typical energy of an emitted photon is $E_\gamma \simeq \gamma\hbar\omega_p$ with the plasma frequency of the corresponding medium $\omega_p = \sqrt{4\pi\alpha n_e/m_e c^2} = 28.8\sqrt{\rho\frac{Z}{A}}$.
Since the transition radiation is related to $\gamma = \sqrt{1/1-\beta^2}$ whereas other energy loss effects depend on β, transition radiation is a great tool to identify particles in higher momenta regions. For the momenta at which particles reach the TRD, electrons are the only particles with $\gamma > 1000$ and therefore produce transition radiation making TR a good tool to identify electrons (see fig. 4.1).
On the other hand, the mean number of emitted transition radiation photons per boundary surface is with about $\frac{1}{137} = \alpha_e$ rather low. Within a TR detector many boundary surfaces are therefore used, realised as foil sequences, micro fibers or other materials providing a large number of boundary surfaces. The number of TR photons is, though, limited and saturates for many boundary surfaces, because of interference effects.

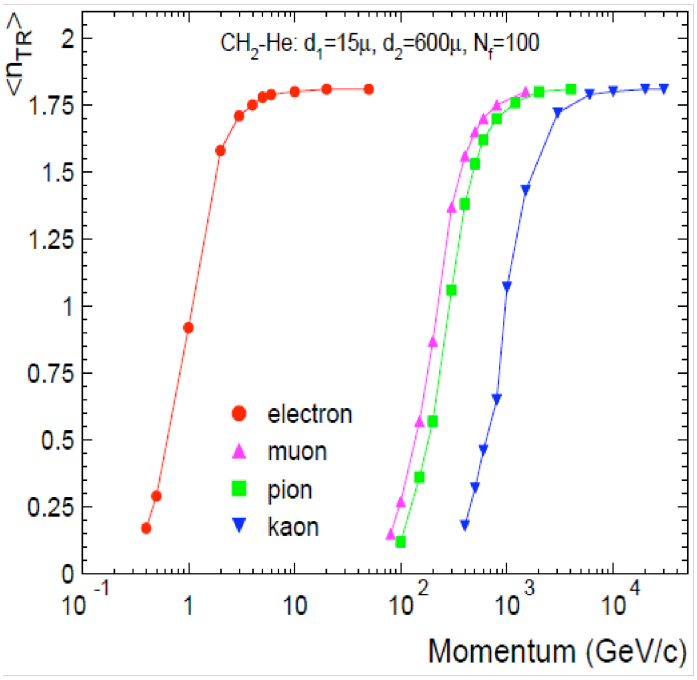

Figure 4.1.: The mean number of transition radiation photons produced by various particles versus momentum. The mean number rises and saturates quickly after a threshold momentum is reached [35].

4.2. The Transition Radiation Detector for ALICE

4.2.1. Setup of the ALICE TRD

The Transition Radiation Detector (TRD) located between TPC and TOF is installed into a mechanically supporting structure named *spaceframe*. The TRD covers a pseudorapidity range of $|\eta| \leq 0.9$ and an azimuth $\varphi = 360°$. In radial direction it is located between 2.9 $m \leq r \leq 3.7$ m from the beam axis [35]. The detector is assembled and installed as 18 individual *supermodules*, each covering an azimuthal segment of 20°. Along with mechanical stability, the supermodule frames provide power supply and cooling for the readout electronics. Each supermodule (SM) contains 30 gas detector chambers, arranged in stacks and layers. In beam direction (z-axis), the SMs are subdivided into 5 stacks, each with 6 layers of chambers in radial direction. For the cylindrical coordinates of the TRD, the chambers are of different size. There are two types of chambers, C0 and C1. The C0 chambers are installed in stack 2 in the middle of the TRD at $\eta = 0$. They have the same length in all layers. The other stacks are filled with C1 chambers. The further outwards the layer, the longer the C1 chambers are in z-direction as well as in φ-direction [35].
In total, the TRD will consist of 540 chambers. The chamber coordinates (x, y, z) are related to the global TRD coordinates (r, φ, z) in the following way: x corresponds to r, y corresponds to negative φ. Chamber z is the same as global z. Figure 4.2 illustrates the configuration.

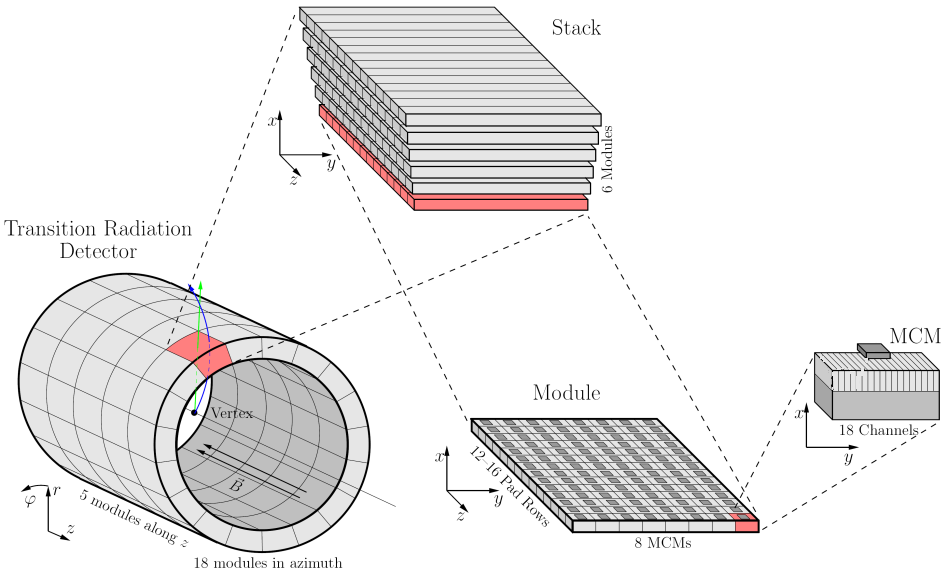

Figure 4.2.: The layout and coordinate systems of the ALICE TRD [34].

4.2.2. Readout Chambers

The 540 detector modules are composed of three parts of different functionality: A radiator, a multi-wire proportional chamber and readout electronics.
The radiator is built in a sandwich structure with two Rohacell foam sheets of 0.8 *cm* thickness and a mat of 3.2 *cm* polypropylene fibers in between. This provides mechanical stability and sufficient Transition Radiation (TR) efficiency at a reasonable thickness [35]. A relativistic particle crossing the radiator generates 1.45 X-ray photons on the average [36]. A detailed explanation of the radiator is given in section 4.2.3.
A readout chamber (ROC) of 3.7 *cm* thickness is mounted on top of the the 4.8 *cm* thick radiator, filled with a detector gas. It is designed as a time projection chamber with a drift volume followed by an amplification region. The chambers will be operated in such a way that they work as time projection chambers with a multi-wire proportional chamber (MWPC) readout. The top of the radiator serves as entrance window and drift electrode to the readout chamber. The drift region is 3 *cm* thick and ends at the cathode wires, set to ground potential.
The design of an ALICE TRD chamber as well as the signal creation is schematically shown in Fig. 4.3.

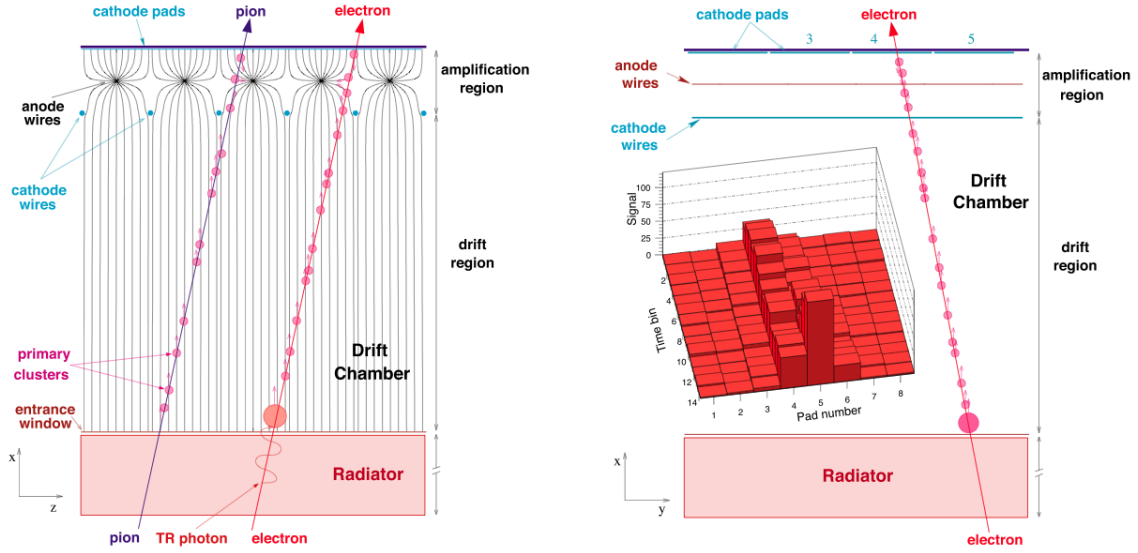

Figure 4.3.: The principle of the ALICE TRD. The left figure shows the projection in the plane perpendicular to the wires. The right figure shows the projection in the bending plane of the ALICE magnetic field. In this direction the cathode plane is segmented into the pads from 0.635 to 0.785 *cm* width. The insert shows the distribution of pulse height over pads and time bins spanning the drift region for a measured electron track [27].

The large cluster at the beginning of the drift chamber originates from a transition radiation photon of the electron. Electrons produced by ionisation energy loss (dE/dx) and by transition radiation absorption drift along the field lines toward the amplification region where they produce avalanches around the anode wires. These avalanches induce a signal on the cathode pads. The insert in the right figure shows the distribution of pulse height over pads and time bins spanning the drift region for a measured electron track. The local coordinate system shown is the coordinate frame of a single readout chamber with the z-direction parallel to the beam axis.
A homogeneous drift field of 700 V/cm is applied, leading to a drift voltage of -2.1 kV. Between the drift wires and the pad plane, a plane of anode wires is installed, typically with a voltage of $+1.5$ kV. Both drift and anode wires are oriented in y-direction. In figure 4.4, the internal geometry is given. Between drift and anode wires, the electric field is inhomogeneous, and electrons passing this region gain enough energy to ionize other gas molecules. An avalanche of electrons is generated, the number of electrons per avalanche is proportional to the applied anode voltage.

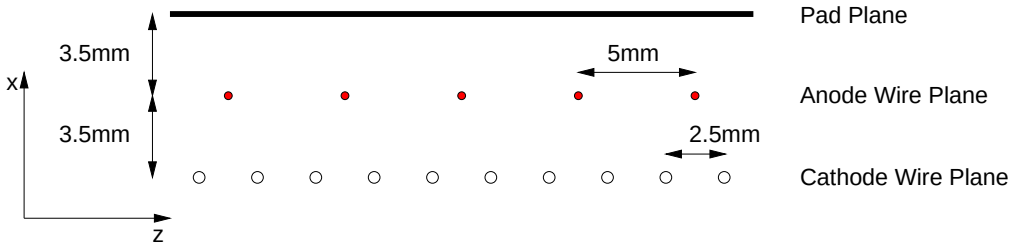

Figure 4.4.: Wire geometry in TRD readout chambers [35].

By this design of a chamber, drift time and signal amplitude are adjusted independently. A higher drift voltage leads to a shorter signal length, a higher anode voltage leads to an increase of the signal amplitude.
The chambers are filled with Xe/CO_2 (85%/15%)[1]. Due to its large atomic number Z, Xe has a high X-ray photoabsorption probability; CO_2 serves as quencher.
On top, facing the readout chamber, a pad plane is mounted. The plane is built of rhomboid shaped Cu-pads with an average length of 7.3 cm in z-direction and 0.9 cm in y-direction [35]. With their average area of 6.3 cm^2, the pads are the smallest unit in the ALICE TRD and determine its granularity.
One layer of a TRD SM comprises 144 pad columns in y-direction and 76 pad rows in z-direction. Stack 2 chambers have 12 rows, all other chambers have 16. Like the drift wires, the pad plane is on ground potential. To improve position resolution in z, the pads are tilted by an angle $\varphi_t = \pm 2°$, opposite in consecutive layers. The x-direction corresponds to the time. It has 30 bins of respectively 100ns, which corresponds to 0.1cm. A draft of the geometry of the TRD readout chambers is shown in figure 4.5.

[1]During the dedicated Krypton calibration run the TRD chambers were filled with Ar/CO_2

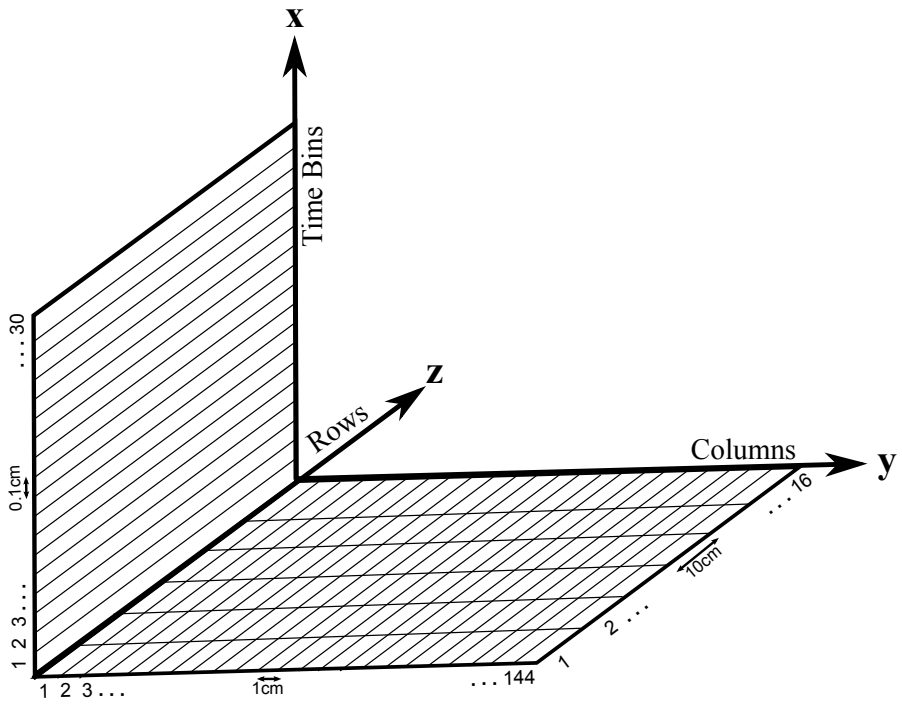

Figure 4.5.: Draft of the geometry of the TRD readout chambers.

The avalanche ionization at the anode wires induces a charge in the pads. The pads are connected to the readout electronics, that record the charge and generate a signal.

4.2.3. Transition radiation in the ALICE TRD

In the sandwich radiator as many boundary surfaces as possible are used to reach a higher yield of transition radiation. Nevertheless, stacks of foils do not provide sufficient mechanical stability and additional supply structures would be needed to strain the foils. The supply structures would lead to large inactive areas which not only reduce the acceptance of the TRD but also spoil the possible results of detectors behind the TRD. The solution found for the ALICE TRD radiator is a combination of foam and fibres providing the optimal combination of TR efficiency and mechanical stability. Figure 4.6 shows the principle design of the radiator sandwich. The supporting structure with good transition radiation production rate is made out of a polymethacrylimide foam, called Rohacell HF71 of 8 mm thickness reinforced by glass fibre sheets. The inner volume of the sandwich cells is filled with polypropylene fibre mats being the main radiator material. Scanning electron microscope images of both materials are shown in Fig. 4.7.

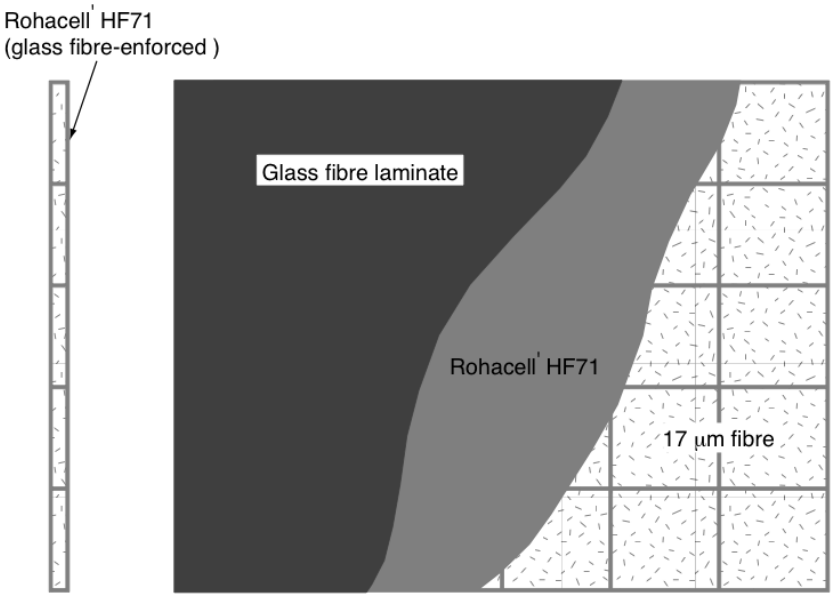

Figure 4.6.: Schematic design of a ALICE TRD sandwich radiator providing the optimal combination of TR efficiency and mechanical stability [27].

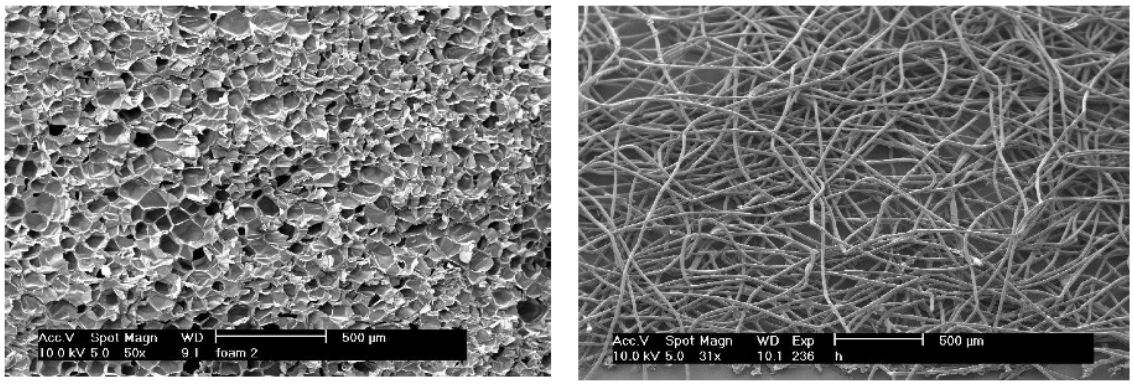

Figure 4.7.: Scanning electron microscope images of the used radiator materials: Rohacell HF71 foam (left) and fibres mat (right) [27].

Since it is challenging to calculate the energy loss of such materials analytically, simulations of the detector response parametrisations are used. In the case of the ALICE TRD the behavior of the radiator is modeled by a foil stack in good agreement with measured results [27].

4.2.4. Front-End Electronics

The chamber Front-End Electronics (FEE) digitize pad signals and calculate *tracklets*. A tracklet is a linear fit of a particle track segment in one Readout Chamber (ROC). As presented in figure 4.8, it can be subdivided into different logical components.

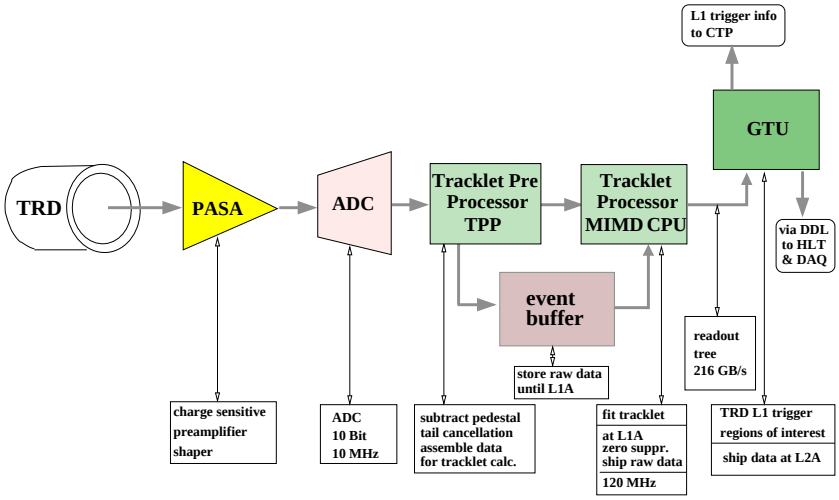

Figure 4.8.: Logical components of the ALICE TRD Front-End Electronics [36].

First, the pad signals are passing a charge sensitive PreAmplifier/ShAper (PASA) and then an Analog Digital Converter (ADC) with a $10MHz$ sampling rate. In a data processing circuit, the data of subsequent time bins is stored in event buffers. During the drift time of the electrons, the Tracklet Pre-Processor (TPP) prepares information for the Tracklet Processor (TP). As part of the TPP, a digital filter is implemented. At the end of the drift time, the TP processes the data of all time bins and determines tracklets. The TP is a CPU implemented as a Multiple Instruction Multiple Data (MIMD) processor, operating at $120MHz$. The ADC, digital filter, TPP and TP are collectively called TRAcklet Processor (TRAP).
These units are mounted directly on the ROCs. The data are then shipped to the Global Tracking Unit (GTU) outside the chambers via optical fibers. The GTU combines the information of the individual TRD ROCs. It receives tracklets from all TRD readout chambers. If there are at least four matching tracklets in one stack, the GTU computes the particle track from the tracklets and sends a positive trigger signal to store the recorded data.
Except for the GTU, all these components are integrated in Multi-Chip-Modules (MCMs) that are mounted directly on the chamber.

4.2.5. Particle Identification with the TRD

Particles entering the TRD drift chamber, as well as transition radiation photons they produced, ionise the gas in the chamber and create electron clusters. The transition radiation photon is absorbed shortly after entering the drift chamber due to the chosen gas mixture. The primary particle constantly generates electron clusters on its way through the chamber.
The final signals produced at the cathode pads as described above are read out at a 10 MHz sampling rate such that the signal height on all pads is sampled in time bins of 100 ns. Figure. 4.9 shows the measured average signals of pions and electrons with and without transition radiation versus the drift time. For small drift times the average pulse height increases rather strongly, it is about twice as high as for time bins in the mid-region. This is due to the signal coming from the amplification region. The following plateau originates from the drift region. The signal from transition radiation of the electrons arrives preferentially later, in higher time bins, since the radiation photons are produced at the entrance of the detector and therefore any signal deriving from them has the longest distance to travel until it is read out.

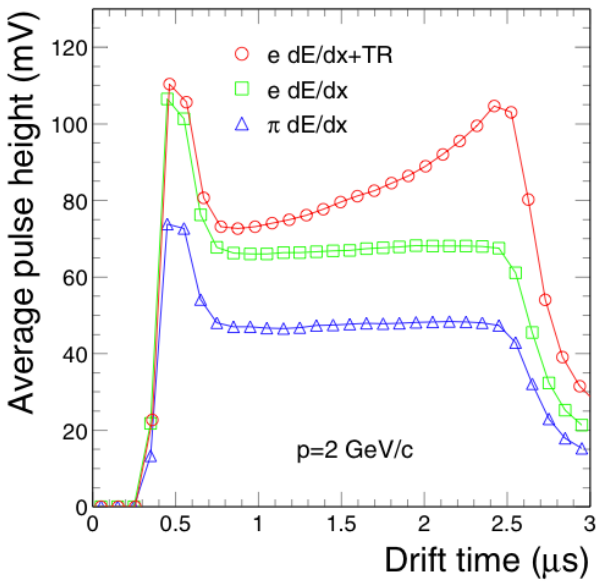

Figure 4.9.: Average pulse height versus drift time for electrons (upper and middle) and pions (lower). The different pulse heights indicate the different ionization energy (dE/dx) loss of electrons (green rectangles) and pions (blue triangles). The characteristic peak at larger drift times of the electron (red circles) is due to the absorbed transition radiation [27].

5. Concept of the Calibration with Krypton

^{83}Kr is an extremely useful isotope for calibrating the response of a proportional counter because it produces electron energy deposition in the important energy range of 9-42 keV [44], which typically corresponds to the dynamic range of a detector of this type. A minimum ionizing particle (MIP) deposits 1.47 $MeV/g\ cm^{-2}$ in Argon gas and 1.23 $MeV/g\ cm^{-2}$ in Xenon gas. Ionization parameters for some common chamber gases are presented in table 5.1.

Gas	Z	A	$\rho\ [g\ cm^{-1}]$	$\frac{dE}{dx}\ [\frac{MeV}{g\ cm^{-2}}]$
Ar	18	39.9	1.66×10^{-3}	1.47
CH_4	10	16	6.74×10^{-4}	2.21
He	2	4	1.66×10^{-4}	1.94
Ne	10	20.2	8.39×10^{-4}	1.68
CO_2	22	44	1.86×10^{-3}	1.62
Xe	54	131.3	5.49×10^{-3}	1.23

Table 5.1.: Ionization properties of some commonly used drift chamber gases. Ionization yields are given for minimum ionizing particles [41].

The technique of using ^{83}Kr as a calibration source first came from the ALEPH experiment in the context of a gain calibration of their hadron calorimeter, as well as monitoring the response uniformity throughout the device [42]. DELPHI also used ^{83}Kr for the same purpose [43]. Most recently the Time Projection Chamber (TPC) of the NA49 experiment [37] and afterwards the ALICE TPC have made use of ^{83}Kr to perform a gain calibration. Within this diploma thesis the gain calibration with ^{83}Kr was performed for the first time for a Transition Radiation Detector (TRD).

5.1. Krypton properties

The $^{83}_{37}$Rb decays by electron capture with a half-life of 86.2 days to excited states of $^{83}_{36}$Kr. In 91% of the cases levels are populated that decay through the isomeric (metastable) ^{m83}Kr level at 41.6 keV with a half-life of 1.83 hours or through the 9.41 keV level with a half-life of 155.1 ns. In 6.4% of the cases the 9.41 keV level is populated directly. The 41.6 keV level subsequently also decays through the 9.41 keV level. The decay scheme is visualized in figure 5.2.
The decay of these two levels are described in more detail in order to understand the Krypton spectrum. They both predominantly de-excite via internal conversion (IC), with a ratio of electron to photon emission e/γ of 2035 for the decay to 41.6 keV level level and of 1709 for the decay to the 9.41 keV level.
Internal conversion (IC) processes transfer the energy of an excited nucleus to a bound shell electron, which then is ejected from the atom with an energy of

$$E_e = E_\gamma - E_b \tag{5.1}$$

where E_b is the binding energy of the electron in its shell and E_γ the excitation energy. Thus electrons with different energies are emitted, depending on their originating shell.
A detailed description of the ^{83}Kr decay spectrum can be found in [44].

The Krypton decay properties are summarized as following:

- **41.6 keV:**
  This energy is due to the summed cascade decay of the 41.6 keV and 9.4 keV level, where the probability is high that no K-shell fluorescence or 9.4 keV photon emission occurs. Due to the short lifetime of the 9.4 keV level the summed decay energy is collected in one cluster.

- **29 keV:**
  Two processes create this energy: the sum of the 9.4 keV and the ca. 19.5 keV electron energy where K-shell fluorescence (whose photons escape) occurs; and the 32.1 keV from the 41.6 to 9.4 keV electrons, where the subsequent 9.4 keV to ground state decay takes place via γ-emission that escapes.

- **19.6 keV:**
  K-shell fluorescence occurs, whose photons escape, as well as the photon from the 9.4 keV decay. This is just like the first case as for the 29 keV energy with the difference that the 9.4 keV level decays via (escaping) photon emission.

➢ **12.6 keV:**
This energy causes from conversion of the K-shell photons in the chamber gas.

➢ **9.4 keV:**
Either conversion of a 9.4 keV photon or the summed 9.4 keV electron energy with the preceeding 32.1 keV transition seperated from it.

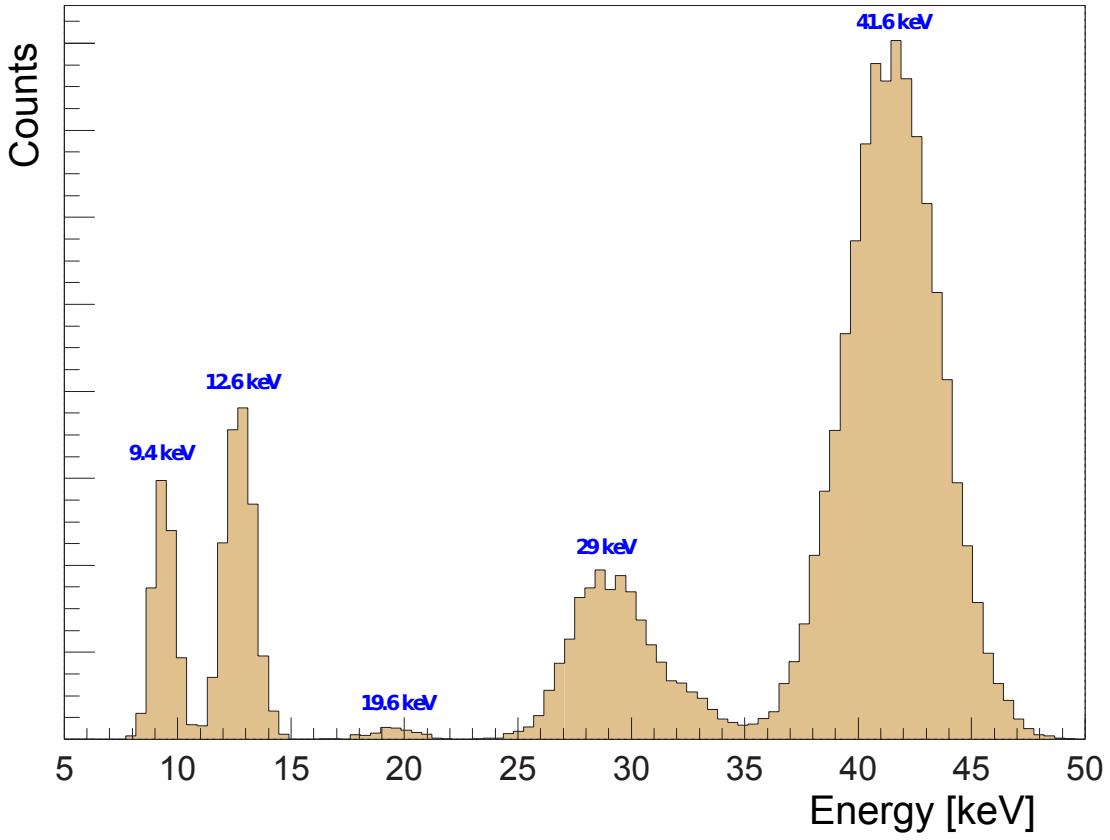

Figure 5.1.: Theoretical draft of the ^{m83}Kr decay spectrum.

Figure 5.1 shows a theoretical draft of the Krypton decay energy spectrum with a resolution of 15%. The energy levels as discussed above are clearly visible.

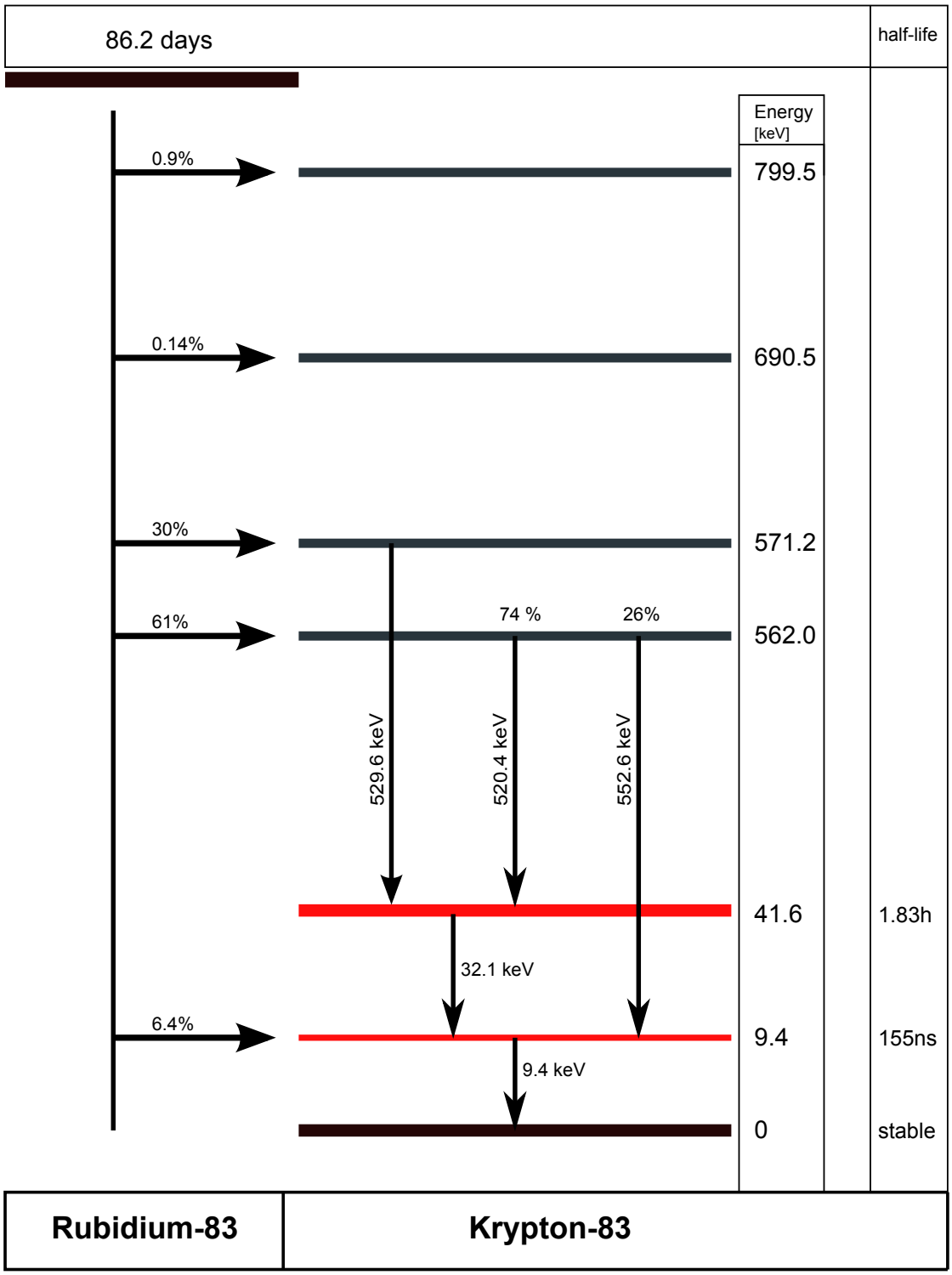

Figure 5.2.: The decay of ^{83}Rb to ^{83}Kr by electron capture. Shown are the most prominent level transitions. The isomeric state ^{m83}Kr at an energy level of 41.6 keV is used for calibration.

5.2. Range of Krypton electrons

In contrast to an electron produced from p-p or Pb-Pb collisions, an electron produced from a Krypton decay has a very short trajectory. Depending on its energy, electrons coming from the decay of Krypton covers a certain distance in the gas, suffering elastic and inelastic scatters with the gas molecules. The total range R_T of charged particles for an energy E, along the trajectory, can be calculated integrating the Bethe-Bloch formula Eq. (4.1) over the length R_T and requiring the integral to equal the total available energy; however, it gives a bad representation of the distance effectively covered by an electron, because of the randomizing effect of the multiple collisions. It is customary to define a practical range R_P that appears to be two or three times smaller than the total range and in general is the result of an absorption measurement.
The practical range of electrons can be calculated using the empirical relation [41]:

$$R_p(E_{kin}) = \frac{A \cdot E_{kin}}{\rho}(1 - \frac{B}{1 + CE_{kin}}) \tag{5.2}$$

where E_{kin} is the kinetic energy of the electron in keV, ρ the gas density in g cm^{-3} and the constants are A $= 5.37 \cdot 10^{-4}$ g cm^{-2} keV^{-1}, B $= 0.9815$ and C $= 3.123 \cdot 10^{-3}$keV^{-1}.
For the TRD gas mixture that was used during the dedicated Krypton calibraion run Ar/CO_2(85%/15%), $\rho_{Ar/CO_2} = 1.8134 \cdot 10^{-3}$ g cm^{-3}.
The range R_p of electrons in the TRD gas mixture, under normal conditions, is shown as a function of energy in figure 5.3. The range of electrons coming from the ^{m83}Kr decay and their corresponding dimensions are summarized in 5.2.
The range of the most prominent energy of E = 41.6 keV is $R_p \approx 1.8$ cm. In the TRD chamber geometry, as described in section 4.2.2, it equates to 1-2 pads in row direction, 2-3 pads in column direction and 19-20 bins in time direction.

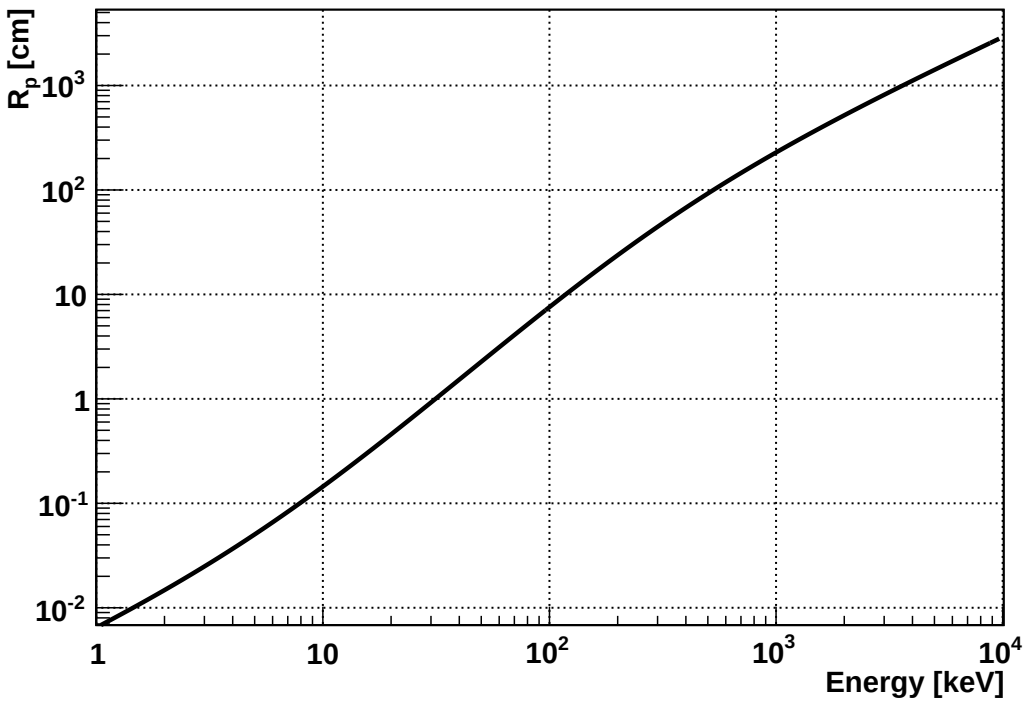

Figure 5.3.: Range R_p of electrons, at normal conditions in the TRD gas mixture of Ar/CO_2, as a function of energy.

E_{kin} $[keV]$	R_p $[mm]$	*Pad columns*	*Pad rows*	*Time bins*
9.4	1.5	1-2	1-2	2-3
12.6	2.3	1-2	1-2	3-4
19.6	4.2	1-2	1-2	5-6
29	9.8	1-2	1-2	10-11
41.6	18.2	2-3	1-2	19-20

Table 5.2.: Range R_p of electrons with energies corresponding to the ^{83}Kr decays in the TRD gas mixture with corresponding dimensions in the geometry of the TRD chambers.

6. Experimental Setup

In this chapter the experimental setup of the ALICE TRD gain calibration using ^{83}Kr is discussed. In section 6.1 the hardware setup is described. The source of ^{83}Kr, which is ^{83}Rb is discussed in section 6.2. In section 6.3 the first day installation and occurring challenges are explained. Section 6.4 gives an overview of the taken data.

6.1. Hardware Setup

The solid ^{83}Rb source was inserted into the TRD gas system via a bypass line. After opening the valves, the decayed gaseous ^{83}Kr disperses in the chambers and decays to electrons with kinetic energies of 9-42 keV, see chapter 5.1. These electrons ionize the gas along their path. The positively charged ions drifts towards the pad plane and a signal is induced. The signal which corresponds to the energy of one ^{83}Kr decay level is distributed on few pads, see 5.2. Figure 6.1 shows a schematic view of the experimental setup.

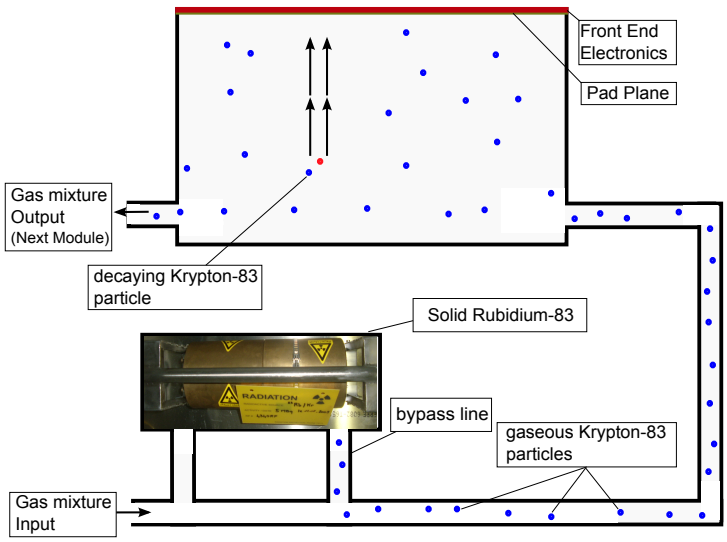

Figure 6.1.: Schematic view of the experimental setup showing one TRD chamber connected to the gas system.

6.2. The Rubidium ($^{83}_{37}$Rb) source

The Rubidium Source shown in figure 6.2 was produced on the 12^{th} of August 2009 at the Isotope Separator On Line-DEtector (ISOLDE) at CERN.

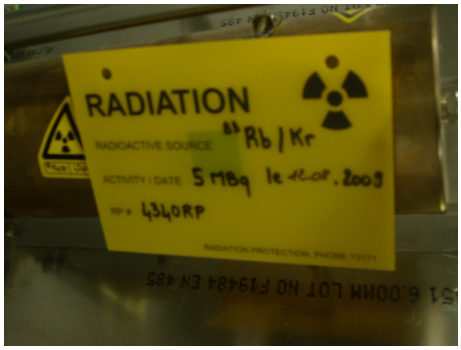

Figure 6.2.: Picture of the ^{83}Rb source.

The ^{83}Rb source was available for the TRD on the 28^{th} of August 2009. The data taking started, when the bypass line was opened, on the 31$^{\text{st}}$ of August 2009 and ended on the 21$^{\text{st}}$ of September 2009.
The source was produced with a maximum activity of 5 MBq. Figure 6.3 shows the activity of the Rubidium source as a function of time.

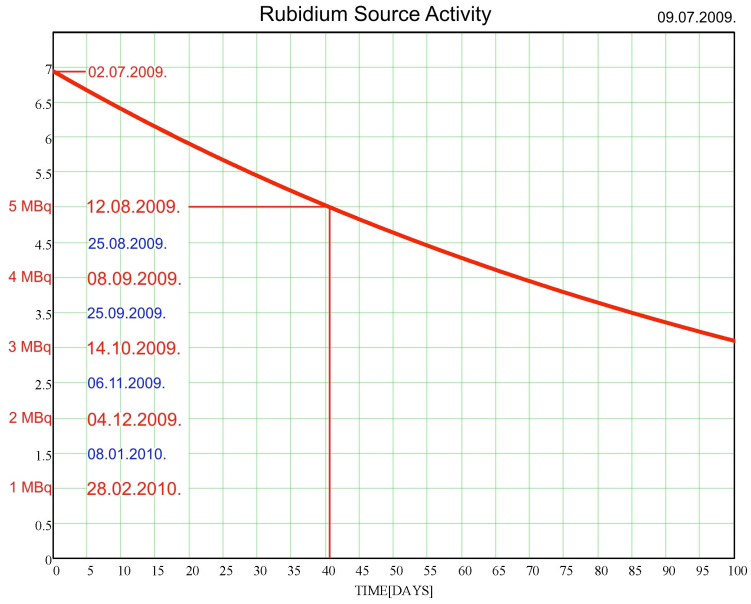

Figure 6.3.: The activity of the Rubidium source as a function of time [40].

6.3. First day installation and data taking

On the 31^{st} of August 2009, the Rubidium source was installed in the bypass. At 6:40 p.m the valves were opened and the gaseous ^{83}Kr distributed in the TRD chambers.
After accumulating some statistics, the behavior of Krypton was surveyed. Figure 6.4 shows that the ^{83}Kr was only distributed in these layers, where chambers are next to the gas inject (lower layers). Figure 6.5 shows a screenshot of the TRD control system showing the anode high voltage current of one chamber as a function of time. The current increases rapidly after opening the valve of the source and then decreases exponentially. This is due to the fact that the source was closed for some hours before connecting it to the TRD gas system. Thus quite some activity was gathered which then was at once released to the chambers. After the exponential decay some chambers went back to zero, other remain at an offset of a few tens of nA.

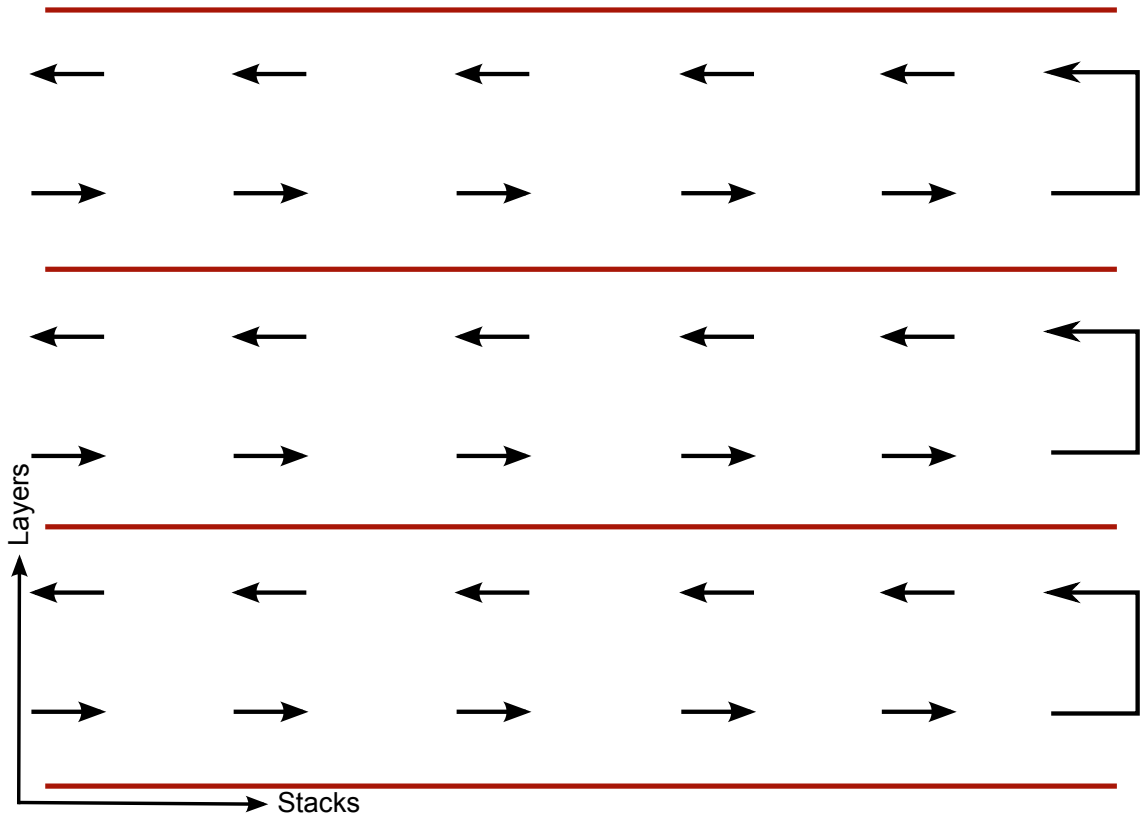

Figure 6.4.: Cluster distribution in all chamber in sector 1. It shows that only layers, where chambers are next to the gas inject (lower layers) are filled by Krypton. The arrows illustrates the gas circulation in the TRD [47].

Figure 6.5.: Screenshot of the Graphical User Interface (GUI) of the TRD control system showing the anode high voltage current of one chamber as a function of time (red line). Only layers next to gas inject are filled by Krypton, this is visible in the green box due to the low current (IAnode=0.001) of L1, L3 and L5 [48].

After investigations, the conclusion was that ^{83}Kr decays before it reaches the last chambers in each loop. Therefore the gas flow into TRD modules was increased by 50%. Afterwards all chambers showed significant statistics.

6.4. Data and Statistics

Before connecting the source to the TRD gas system, the duration of the data taking was estimated. Therefore a calculation was carried out to determine the minimum number of ^{83}Kr decays necessary. From the minimum needed ^{83}Kr decays, the source activity and the TRD specifications, one can get the minimum needed duration of the calibration run. These calculations are introduced in this section.
Seven sectors, the so called supermodules (SM), were installed in the ALICE setup in 2009 with the full data readout chain and participated in the Krypton calibration data taking. The installed sectors and their chamber range are listed in table 6.1.

TRD Sector	Chambers No.
0	0 - 29
1	30 - 59
7	210 - 239
8	240 - 269
9	270 - 299
10	300 - 329
17	510 - 539

Table 6.1.: The installed TRD sectors in the ALICE setup in 2009.

The data taking started on the 31st of August 2009 and ended on the 21st of September 2009.

The number of pads in the installed supermodules is:

$$N_{SM} \times N_{Layers/SM} \times N_{Pads/Layer} = 7 \times 6 \times (76 \times 144) = 459648 \text{ pads.} \quad (6.1)$$

where N_{SM} is the number of installed TRD super modules during the 2009 calibration data taking period, $N_{layers/SM}$ is the number of layers per super module and $N_{Pad/Layer}$ is the number of pads per layer.
In order to measure the ^{83}Kr energy spectrum a minimum number of ca. 2000 ^{83}Kr clusters per pad is needed. This means that a minimum amount of ca. one billion ^{83}Kr clusters is required:

$$N_{Pads} \times N_{clusters/Pad} = 459648 \times 2000 \approx 1 \cdot 10^9 \text{clusters.} \quad (6.2)$$

where N_{Pads} is the number of pads and $N_{clusters/Pad}$ is the number of minimum needed clusters per pad.

The TRD can detect, with the average source activity, up to:

$$\bar{A} \times R \times f \times P_{decay} = 2.5 \cdot 10^{6} \times 3 \cdot 10^{-6} \times 1 \cdot 10^{-6} \times 70\% = 5250 \ \frac{\text{decays}}{\text{s}} \quad (6.3)$$

where $\bar{A}$ is the average activity of the ^{83}Rb source per second , R is the detector resolution in s, f is the trigger frequency in Hz and P_{decay} is the branching ratio of the most prominent ^{83}Kr decay.
In order to calibrate the TRD on a pad level using Krypton, a minimum data taking period of $1 \cdot 10^{9}$ decays/5250 decays s^{-1} $\approx$ 54 hours is estimated.

Beyond the calibration, Krypton allows to understand the correlation between gain and High Voltage (HV) setting, see chapter 8. Therefore data with different HV settings were recorded:

- HV = 1450 V
  130 runs
  552 M events = 2B ^{83}Kr decays

- HV = 1470 V
  51 runs
  196 M events = 0.8B ^{83}Kr decays

The total raw data size is 30TB, which was reduced to 10TB after the reconstruction done at CERN. The data were then transfered from CERN to GRID and then to GSI, where the analysis procedure was ran, see chapter 7.
Figure 6.6 shows the time table of the TRD dedicated krypton calibration. Starting from the source production in the 12^{th} of August 2009 till the end of the Krypton data taking on the 21^{st} of September 2009.

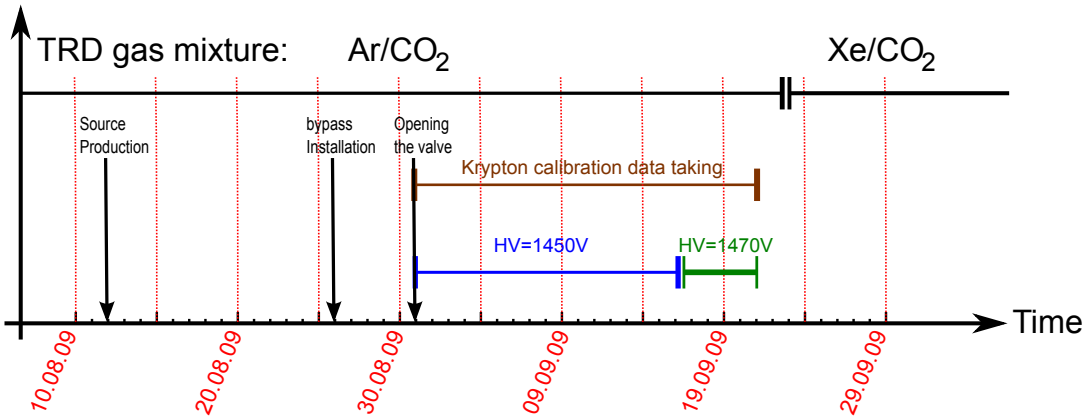

Figure 6.6.: Time table of the TRD dedicated krypton calibration.

7. Analysis

In order to investigate the signal induced by the ^{83}Kr decay a detailed Monte Carlo (MC) simulation was performed. This allows to check the ^{83}Kr cluster size and develop the first analysis macro. This is discussed in detail in section 7.1.
In contrast to MC-simulations, real data contains a large fraction of noise, see section 7.2. Therefore a noise run was recorded and analysed in order to understand its behavior. Cuts for noise reduction were investigated and implemented.
In section 7.3 the analysis strategy and the calibration software, which has been developed within this thesis, are explained. The software is based on the AliRoot framework [45]. This framework, written in the C++ language, is based on the ROOT data analysis software [46]. It contains additional classes providing special functions for the ALICE experiment, e.g. detector simulation, event reconstruction, or gain calibration. At the end of this chapter, in section 7.4, the results of the TRD gain calibration using ^{83}Kr are presented and discussed.

7.1. Monte Carlo simulation

The digitized signals of the readout pads that are above a threshold of 10 ADC-counts are named *digits*. Per event, an algorithm, the so called TRD standard cluster finder, searches into a one dimensional region of seven pad-columns for the digit with the maximum ADC-counts. The ADC-counts of this pad and its two neighboring pads are summed. A so called *cluster* is defined with the position of the pad with maximum ADC-counts and an energy corresponding to the summed ADC-counts. The clusters are illustrated as red dots in figure 4.3.
In order to investigate whether or not to change the existing cluster finder, clusters of electrons produced from p-p or Pb-Pb collisions were compared to electrons produced from ^{83}Kr decays. The results of the performed simulation are shown in figure 7.1. The cluster size of electrons produced from p-p or Pb-Pb collisions are similar but not identical to those produced from ^{83}Kr decays. A cluster of an electron produced from ^{83}Kr decay is typically distributed on 2-4 pads with large energy deposition on each pad. An electron produced from p-p or Pb-Pb collisions generates a cluster up to seven pads. The conclusion was to keep use of the TRD standard cluster finder. However its output, which are reconstructed clusters, is used as an input of a more sophisticated Krypton cluster finder.

In the following paragraph the working principle of the developed Krypton cluster finder is explained.

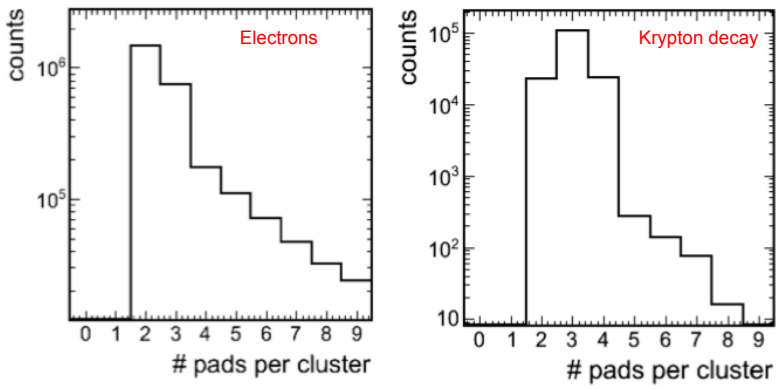

Figure 7.1.: Simulated cluster size reconstructed for electrons (left) compared to those from ^{83}Kr decay (right)

The Krypton cluster has a three dimensional distribution and large energy deposition. Therefore Krypton cluster finder, which has reconstructed clusters as an input, is doing the following, see fig.7.2:

- Find within a chamber the cluster with the maximum value of ADC-counts.
- Search in all three dimensions for neighboring clusters.
- Build the ^{83}Kr cluster, the so called super-cluster, as the sum of all three dimensional adjacent clusters.
- Define the super cluster position as the pad with the maximum energy deposition and it's energy value as the total energy sum.

In order to cross check the developed Krypton cluster finder before having real data, a MC-simulation was performed for ^{83}Kr decays with electron energies of 41.6 keV and 29 keV. The analysis results of the simulated data is shown in figure 7.3. The two simulated electron energies of 41.6 keV and 29 keV appears as two peaks in respectively channel 2570 ADC-counts and 3540 ADC-counts. The distributions below 2400 ADC-counts and above 3800 ADC-counts corresponds to simulated noise. Figure 7.3 demonstrates that the developed Krypton cluster finder is able to reproduce the ^{83}Kr decay spectrum. Furthermore it allows to declare the cluster position three dimensional with a high efficiency.

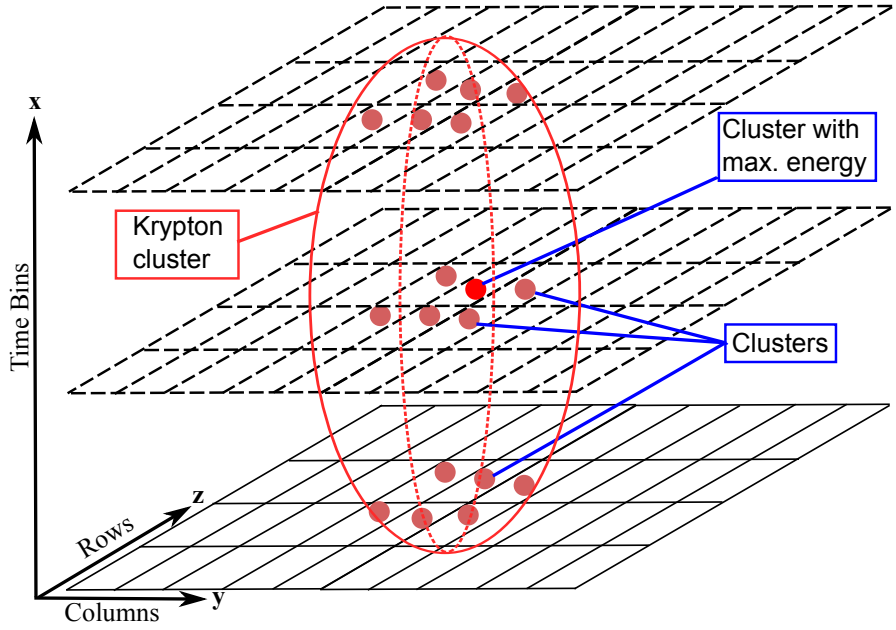

Figure 7.2.: A sketch of the ^{83}Kr cluster finder algorithm.

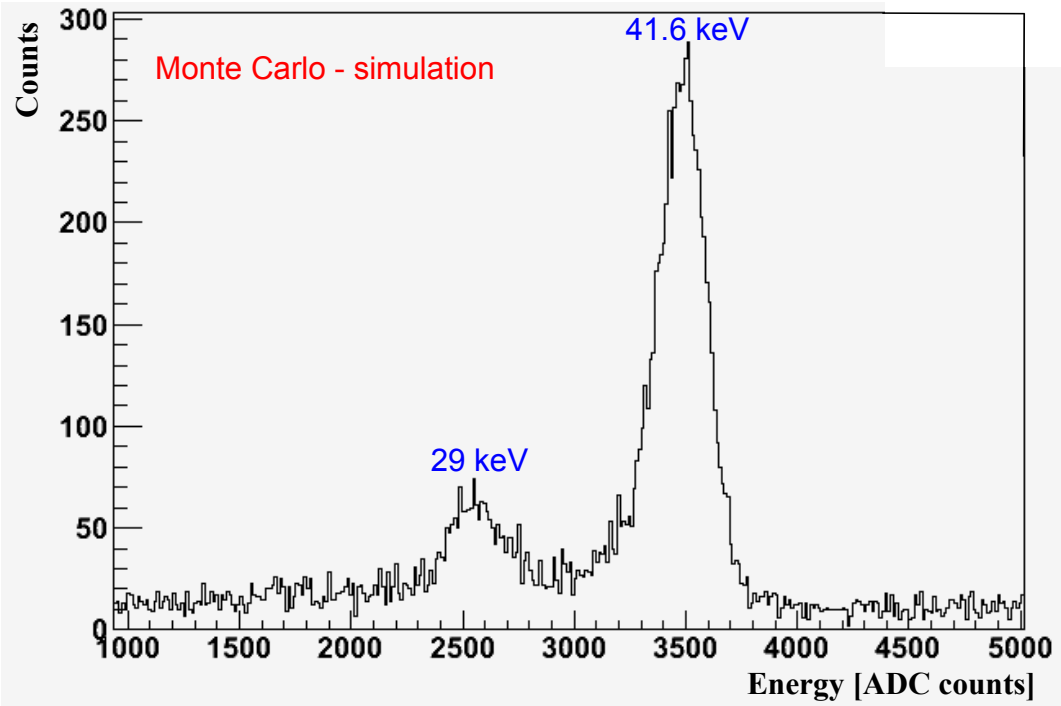

Figure 7.3.: Simulation of ^{83}Kr decays with electron energies of 41.6keV and 29keV.

7.2. Noise

There are two kinds of noise, one is the pedestal, which exists in all electronics and the other type is the pick up noise (coming from outside) normally caused by grounding.

- **Pedestal noise:**
  Electronic noise is a random fluctuation in an electrical signal, a characteristic of all electronic circuits. Noise generated by electronic devices varies greatly, as it can be produced by several different effects. Thermal noise and shot noise are inherent to all devices, while other types depend mostly on manufacturing quality and semiconductor defects.
- **Pick up noise:**
  In electrical engineering, ground or earth may be the reference point in an electrical circuit from which other voltages are measured, or a common return path for electric current, or a direct physical connection to the earth. In electronic circuit theory, a "ground" is usually idealized as an infinite source or sink for charge, which absorbs an unlimited amount of current without changing its potential. Where a ground connection has a significant resistance, the approximation of zero potential is no longer valid. Stray voltages or earth potential rise effects will occur, which may create noise in signals.

7.2.1. Noise cuts

After detailed investigations, two cuts show a stable and good performance for reducing noise.

- **Event cut:**
  The experience shows that some events have a large amount of noise. To exclude using these "bad events" an event cut was implemented. Figure 7.4 shows the cut criteria. The idea is to cut out all events with number of clusters higher than 800. This criteria shows a good performance by removing these betimes noise shots.

- **Cut in rms-time vs energy:**
  Noise is typically randomly distributed in time and has a low energy deposition. A Krypton cluster has a predefined time distribution depending on its size and has typically a higher energy depending on the energy deposition of the corresponding electron. The correlation of the root mean square (RMS) in time dimension of the ^{83}Kr clusters with their energy is shown figure 7.5. The signal is clearly distinguishable from noise thus a cut in two dimensions was applied to remove noise.

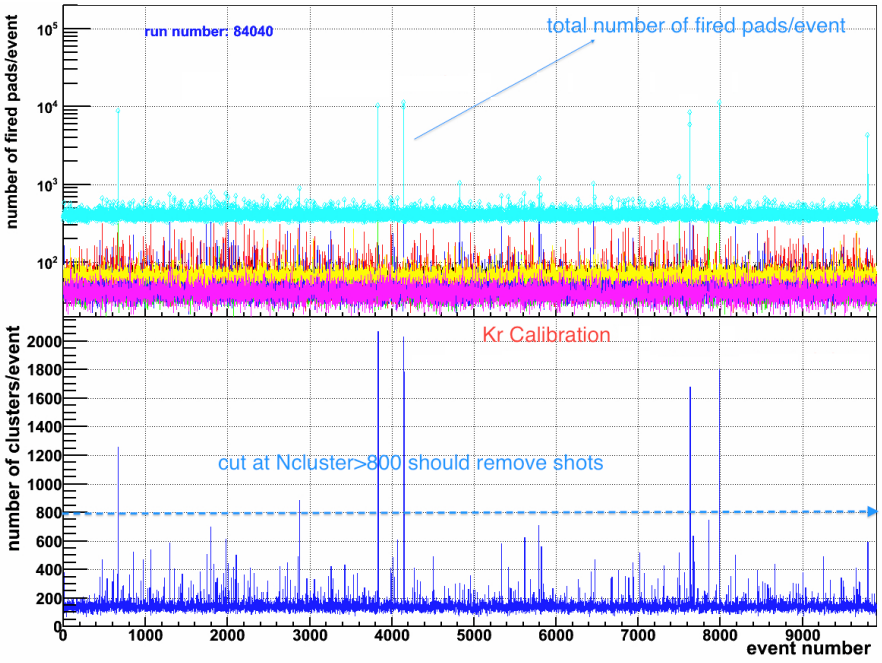

Figure 7.4.: Correlation of pick-up noise with the number of fired pads. The cut to reduce noise is implemented for 800 clusters/event [49].

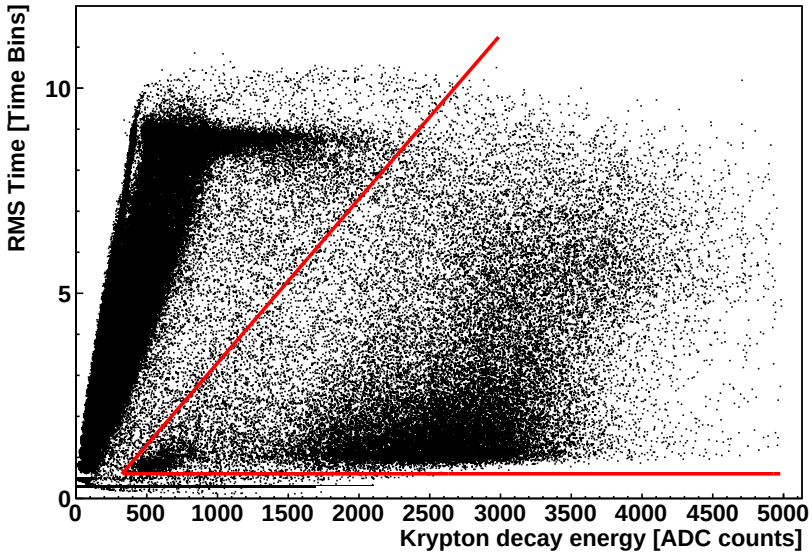

Figure 7.5.: Using the root mean square in time direction versus the energy of the ^{83}Kr decay for noise cuts. The red lines illustrate the cut criteria.

Figure 7.6 shows the ^{83}Kr energy spectrum before applying the noise cuts, which is identical to the projection on the x-axis of the data points of figure 7.5. The ^{83}Kr energy spectrum decreases exponentially in low energy region, E < 1300 ADC-counts, due to high fraction of noise and it peaks around 2400 ADC-counts due to the most prominent ^{83}Kr decay. This spectrum contains a small sample of 0.02% of the total statistics.
Figure 7.7 shows the ^{83}Kr energy spectrum after applying the noise cuts, which is identical to the projection on the x-axis of the data points between the two red lines of figure 7.5. This shows that the noise was significantly, typically by 98%, reduced by applying these cuts, thus the ^{83}Kr energy spectrum is visible.

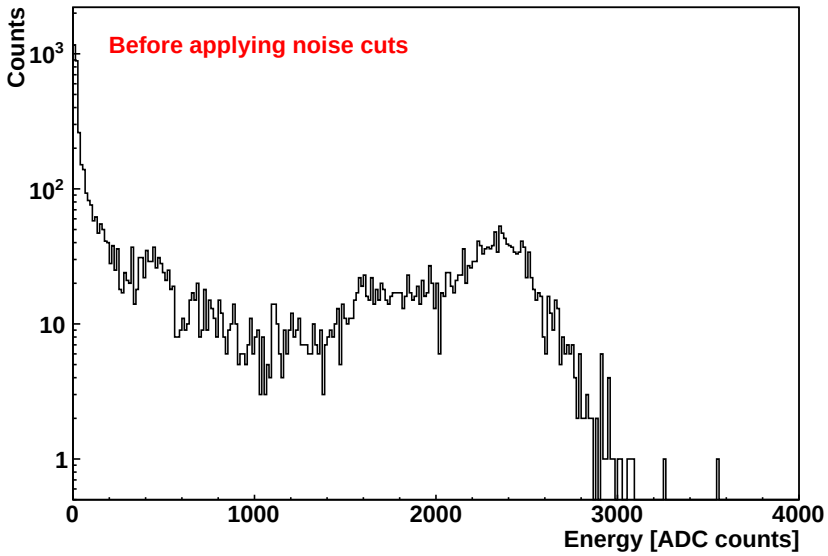

Figure 7.6.: ^{83}Kr energy spectrum for chamber no.241 (Sector 8, Stack 0, Layer 1) *before* applying the cuts for noise reduction. A sample of 0.02% of the total statistics is used.

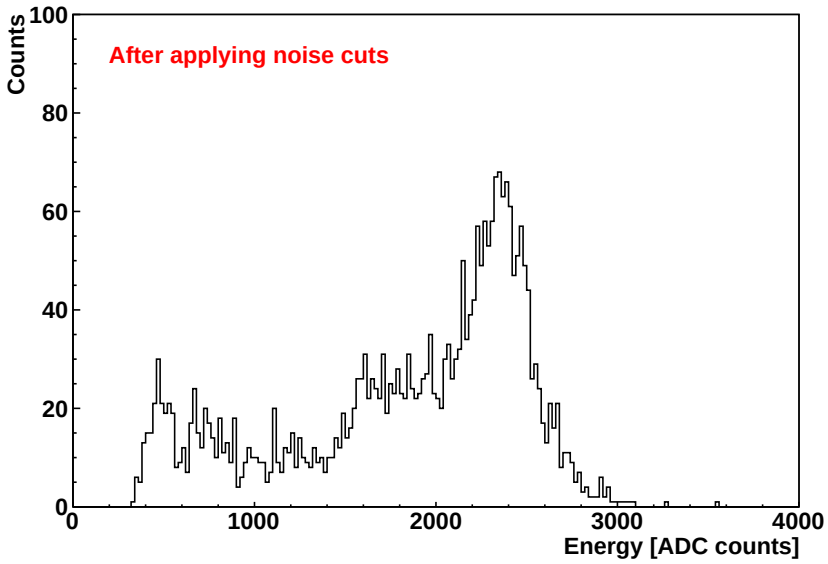

Figure 7.7.: ^{83}Kr energy spectrum for chamber no.241 (Sector 8, Stack 0, Layer 1) *after* applying the cuts for noise reduction. A sample of 0.02% of the total statistics is used.

7.3. Analysis strategy

Beside the present gain calibration using ^{83}Kr, the objective of the developed software package is to provide an automatic procedure to be used in future ALICE TRD gain calibration. The software flow chart of the analysis scheme is shown in figure 7.8 and discussed as follows:

(1) The data from the TRD is shipped to the Global Tracking Unit (GTU), where a random trigger decision is made. The output of the GTU are so-called raw-files that are stored in the ROOT file format *.root. A total raw data size of ca. 30 TB was reconstructed to clusters as described in section 7.1 using the standard TRD cluster finder in the CERN GRID.

(2) Within this diploma thesis a Krypton cluster finder was developed as described in 7.1. Figure 7.9 shows a full explanation of the developed software `AliTRDclusterFinderKr.cxx`. Two scripts `submitBatchAlien.sh`, `runBatchAlien.sh` and a macro `submitData.C` were developed for organizing the data submission and output architecture. The program produces for every data set an energy distribution histogram for each pad, a total of 1.2 millions, and each chamber, a total of 540). This procedure was ran on the GSI Batch Farm, which consists of 1900 computer servers with a total of $\approx$ 8000 CPU.

(3) The output of all data sets, discussed in section 6.4, are merged.

(4) A macro was developed that fits the main peak of all histograms with a Gaussian function and determines the mean position and resolution. The gain parameters of a single pad in a given chamber were calculated as:

$$\mathrm{Gain}_{\mathrm{Pad_i}} = \frac{\mathrm{Mean}_{\mathrm{Pad_i}}}{\mathrm{Mean}_{\mathrm{Chamber}}} \tag{7.1}$$

where $\mathrm{Mean}_{\mathrm{Pad_i}}$ is the mean value of the Gaussian fit of the considered pad and $\mathrm{Mean}_{\mathrm{Chamber}}$ is the mean value of the Gaussian fit of its corresponding chamber.

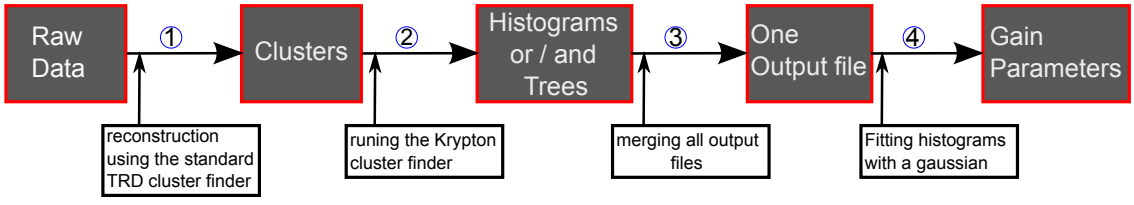

Figure 7.8.: The software flow chart of the analysis scheme, with the four steps.

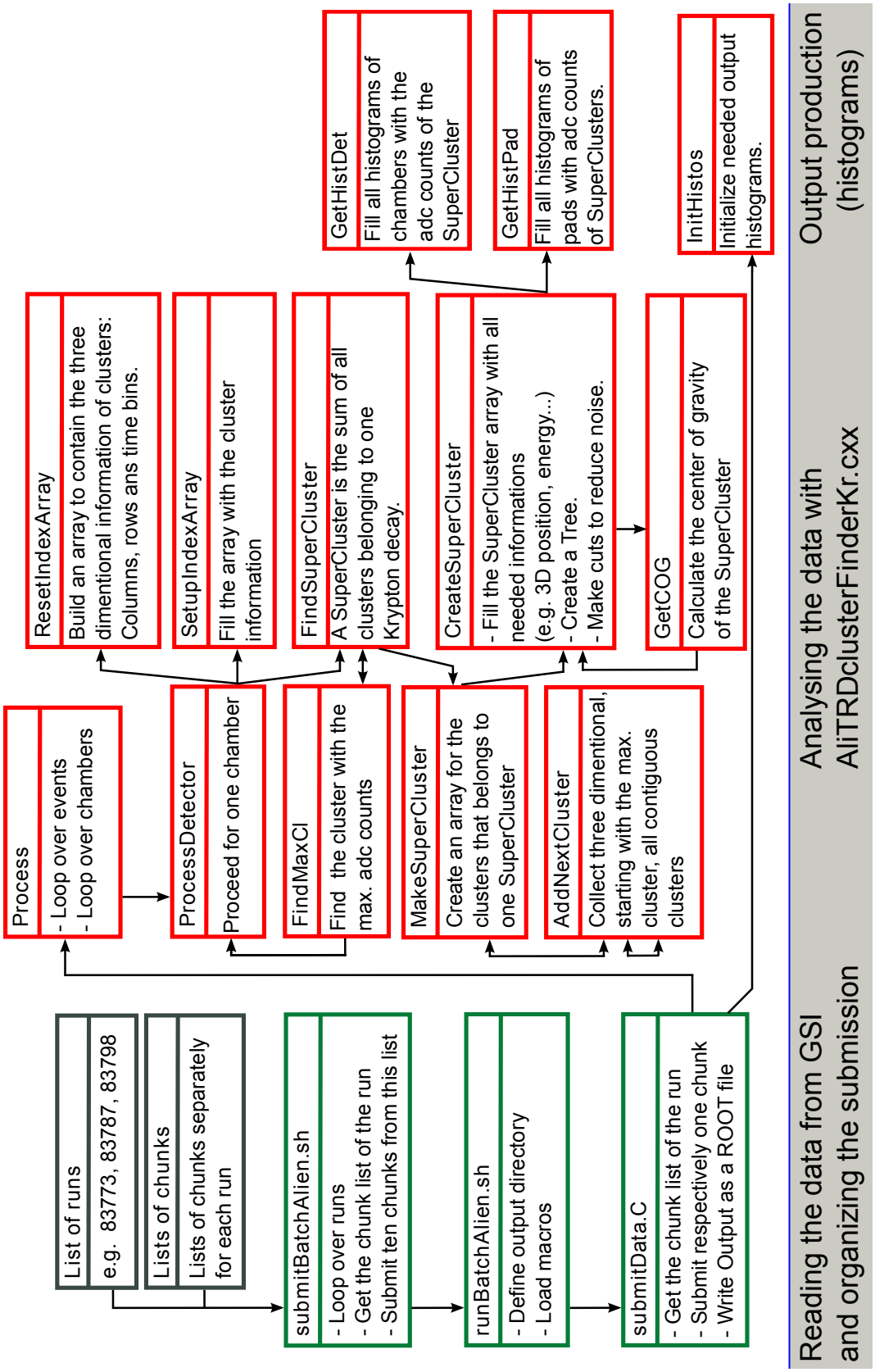

Figure 7.9.: Detailed steps of the developed software package.

7.4. Results

The described analysis strategy has been successfully applied to the recorded data sets. The results are presented in this section.

Figure 7.10 shows the measured Krypton energy spectrum for chamber number 241 (Sector 8, Stack 0, Layer 1). The five ^{83}Kr decay channels described in section 5.1 are clearly visible. The red curve shows the Gaussian fit used as described in 7.3 in order to determine the mean value. The main peak has a mean value of 2280 ADC-counts and a resolution of 420 ADC-counts.
The non-Gaussian tails of the distribution around 300 ADC-counts and 2800 ADC-counts are due the slightly remaining noise. Since relative difference is of our interest, this low background is insignificant for this study.

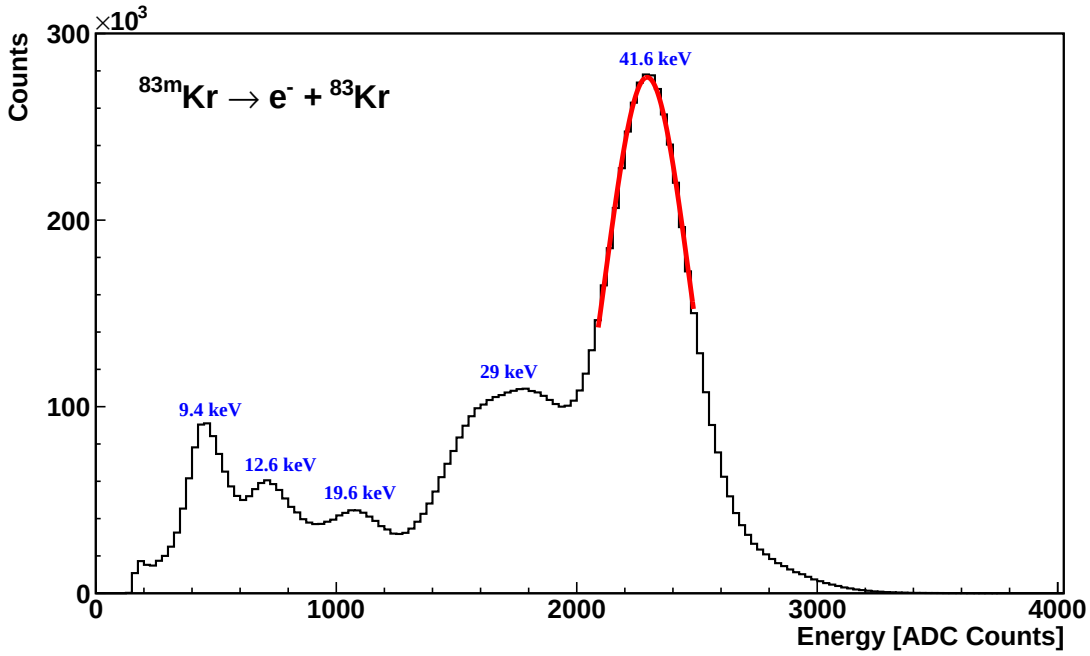

Figure 7.10.: Krypton decay energy spectrum of chamber 241. The ^{83}Kr decay channels as described in section 5.1 are visible. The red curve shows the Gaussian fit procedure.

The fluctuation of the mean value of the Gaussian fit for all installed TRD chambers as a function of chamber number is shown in figure 7.11. The mean values fluctuate within 12.3%, which is consistent with the TRD design specification [35].
The red lines in figure 7.11 separate the different installed TRD sectors.

Six chambers have low mean values. This is due to the fact that these chambers showed large currents and thus were set to lower values of high voltage during the dedicated calibration run.
The spectra of two of these chambers is shown in figure 7.12.

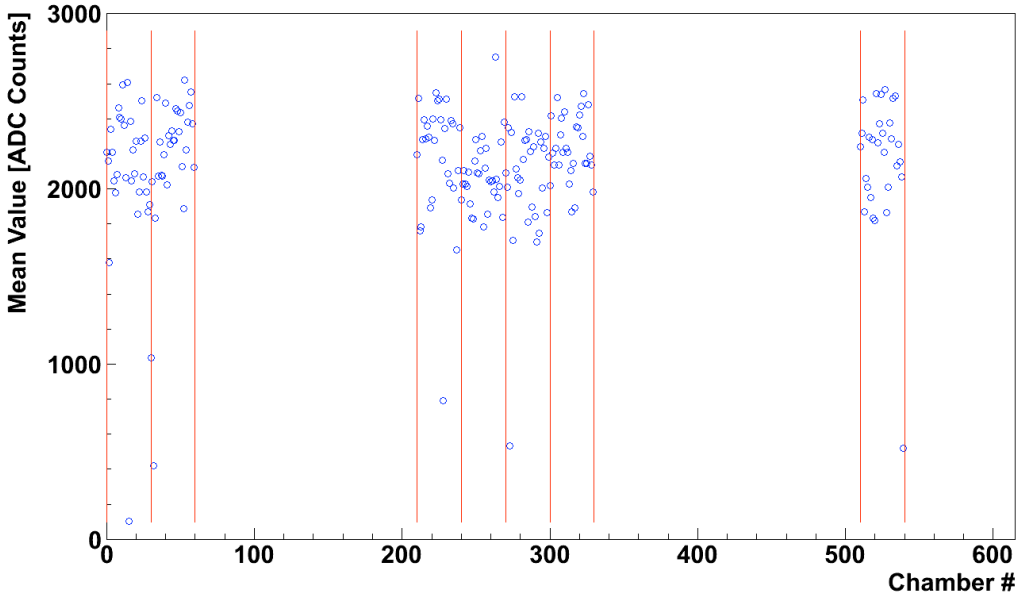

Figure 7.11.: Mean value of the Gaussian fit of the ^{83}Kr spectrum main peak for all installed chambers. The vertical lines separate different TRD sectors.

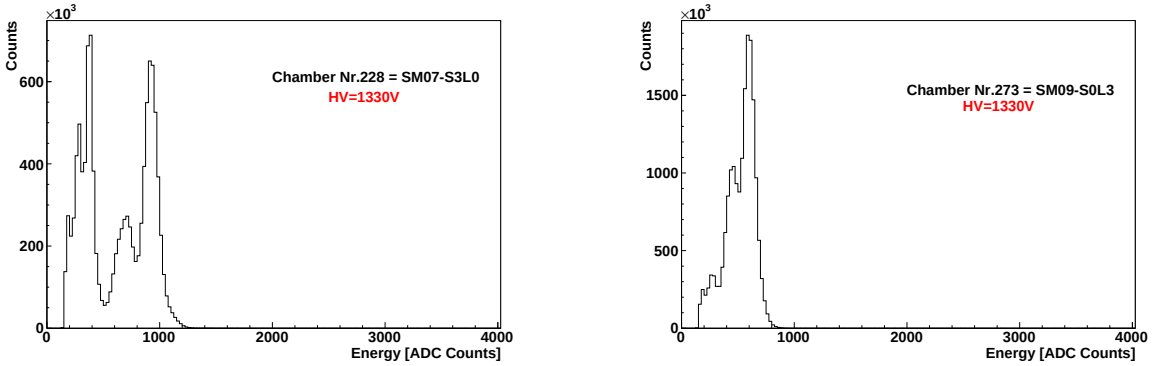

(a) (b)

Figure 7.12.: ^{83}Kr decay energy spectrum: (a) For chamber # 228 (Sector 7, Stack 3, Layer 0) and (b) for chamber # 273 (Sector 9, Stack 0, Layer 3). These chambers had a lower high voltage setting of 1330V during the dedicated calibration run.

Figure 7.13 shows the sigma values of the Gaussian fit for all installed TRD chambers as a function of chamber number. The values, which are proportional to the detector resolution, flactuates within 5.3%. This value consists as well with the TRD design specifications [35].
The red lines in figure 7.13 separate the different installed TRD sectors.

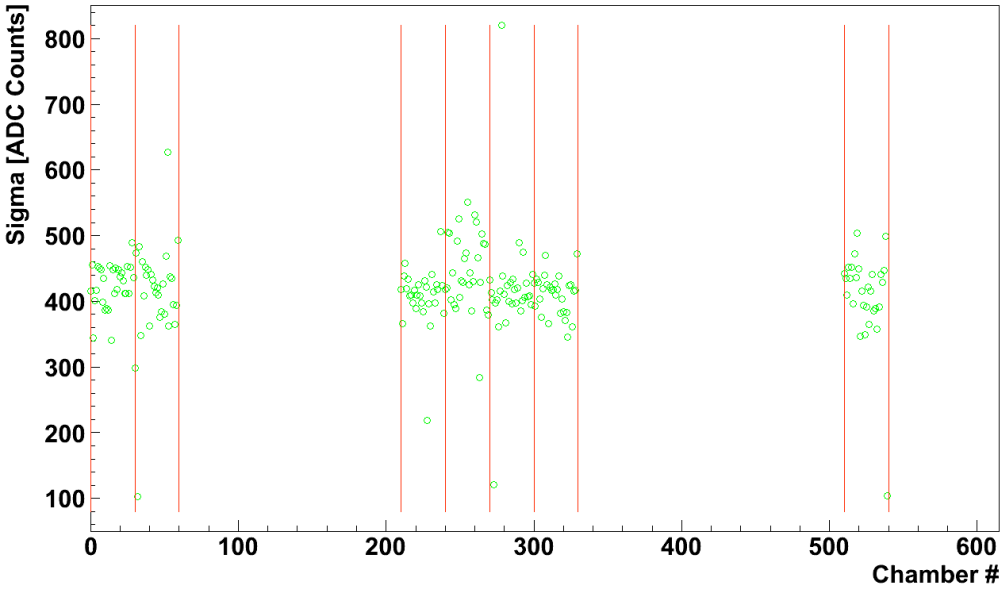

Figure 7.13.: Sigma value of the Gaussian fit of the ^{83}Kr spectrum main peak for all chambers. The vertical lines separate different TRD sectors.

Figure 7.14 shows the measured ^{83}Kr energy spectrum for one pad (Sector 8, Stack 0, Layer 1, row 4, column 116). The five ^{83}Kr decay channels described in section 5.1 are visible. Due to the low statistics, compared to histograms summed over a whole chamber, the corresponding peaks are less clear than in figure 7.10. The red curve shows the Gaussian fit used as described in 7.3 in order to determine the mean value. The main peak has a mean value of 2205 *ADC Counts* and a sigma value of 390 *ADC Counts*.
This fit procedure has been performed for each pad of all TRD installed chambers. Figure 7.15 shows the gain distribution in chamber 241 shows (Sector 8, Stack 0, Layer 1). The gain fluctuates within 12.7%, which is consistent with the TRD design specification [35]. Gain variation on the pad level are seen for the first time in ALICE TRD .

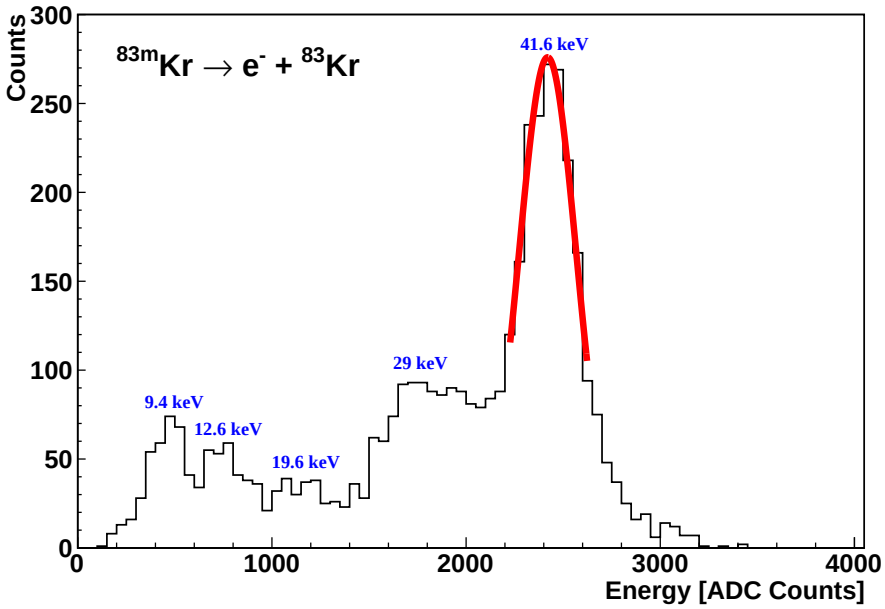

Figure 7.14.: Krypton decay energy spectrum of one pad (Sector 8, Stack 0, Layer 1, row 4, column 116). The red curve shows the Gaussian fit procedure.

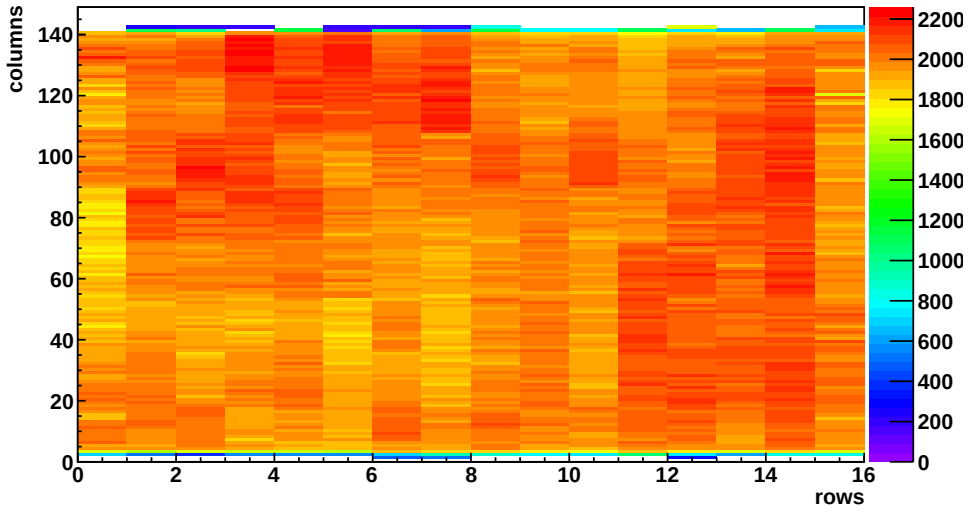

Figure 7.15.: Mean value of the Gaussian fit as a function of pad position for chamber 241 (Sector 8, Stack 0, Layer 1).

The gain factors are extracted from the mean value of the Gaussian fit as described is section 7.3. Figure 7.16 shows the distribution of the gain factors for all pads of the installed TRD chambers. The Gaussian fit has a mean value, which corresponds to the relative gain, of 1.16 ± 0.004 and a sigma of 0.2 ± 0.001 in unit of relative gain. The non Gaussian tails of the distribution describes pads on the chambers border. These, depending on their chamber geometry, have lower or higher gain. The small peak by 0.2 is due to chambers that had a lower high voltage setting during the calibration run.

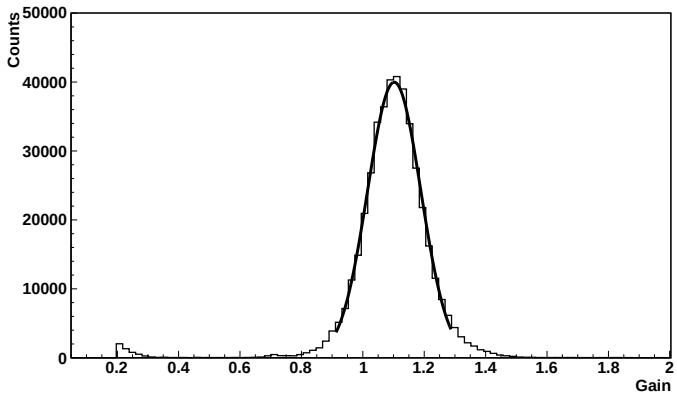

Figure 7.16.: Gain distribution of pads in all chambers.

Figure 7.17 shows the gain distribution for all pads of chamber # 241 (Sector 8, Stack 0, Layer 1). The gain fluctuates at 1 relative unit, so that the Gaussian fit has a mean value of 1.01 ± 0.001 and a sigma value of 0.15 ± 0.001 relative gain unit. Both values consists with the TRD design specifications [35].

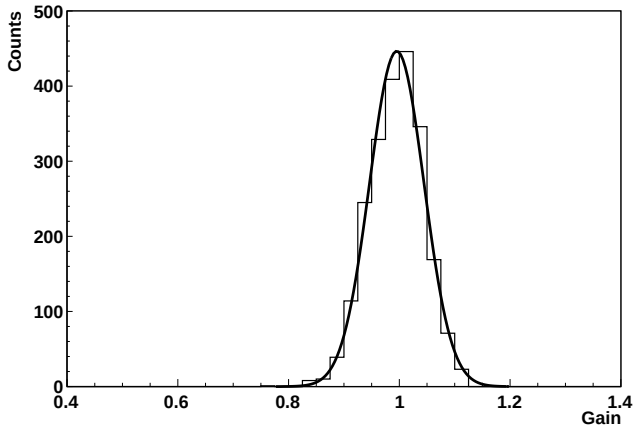

Figure 7.17.: Gain distribution of chamber # 241 (Sector 8, Stack 0, Layer 1).

7.5. Gain Geometry of the TRD chambers

In this section the investigation of the TRD chambers gain geometry is discussed. Due to various reasons such as transportation, installation etc., chambers typically bends in order of few μm. The determined gain factors for each pad using the ^{83}Kr calibration method allow a deeper view of the gain distribution within a given chamber and from it to the understanding of its geometry.
Figure 7.18 shows the gain distribution within chamber #55 (Sector 1, Stack 4, Layer 1). The gain fluctuates within 16%.The chamber has higher gain on the middle left side and lower gain at the borders, especially on the right side. Figure 7.19 shows the gain projection in column direction. The gain has a maximum value of ≈ 1.5 in columns 80-100 and decreases to lower values on the chamber borders. Figure 7.20 shows the gain projection in row direction. The gain has a maximum value of ≈ 1.35 in rows 2-4 and decreases reaching lower values on the right side of the chamber, rows 14-16, than on its left side. The red boxes in figure 7.18 illustrates these projection areas.
This view reflects that the chamber is bent in a way that the middle left side is higher than the other regions of the chamber.

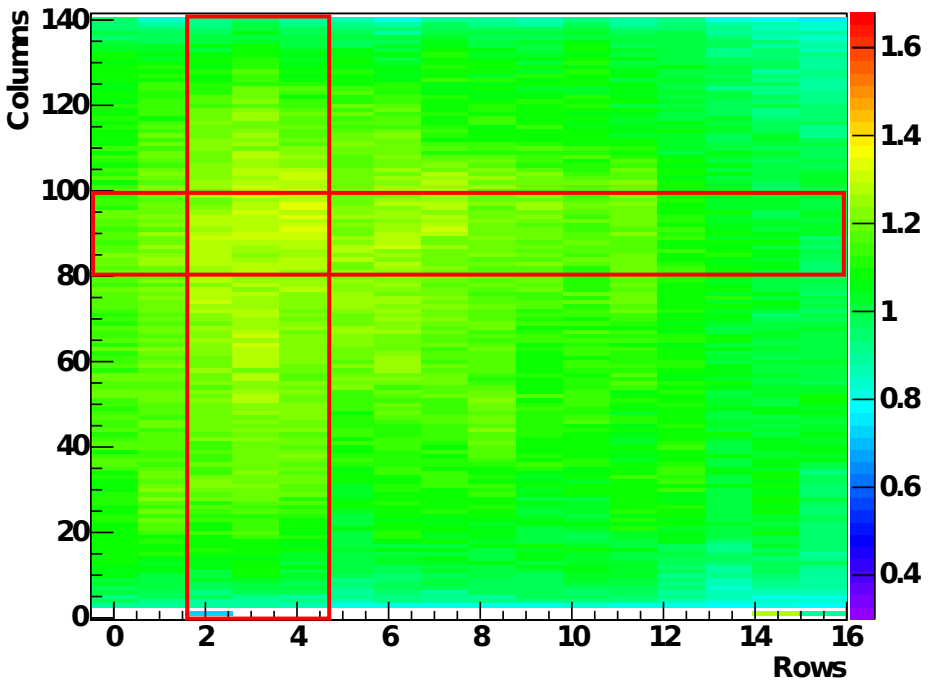

Figure 7.18.: Gain as a function of pad position for chamber #55 (Sector 1, Stack 4, Layer 1).

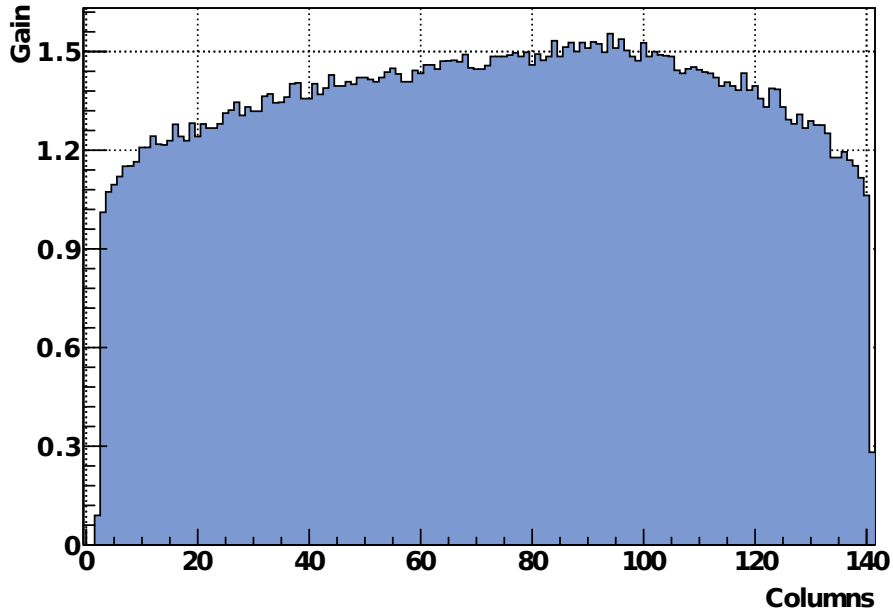

Figure 7.19.: Projection.... for chamber # 55 (Sector 1, Stack 4, Layer 1).

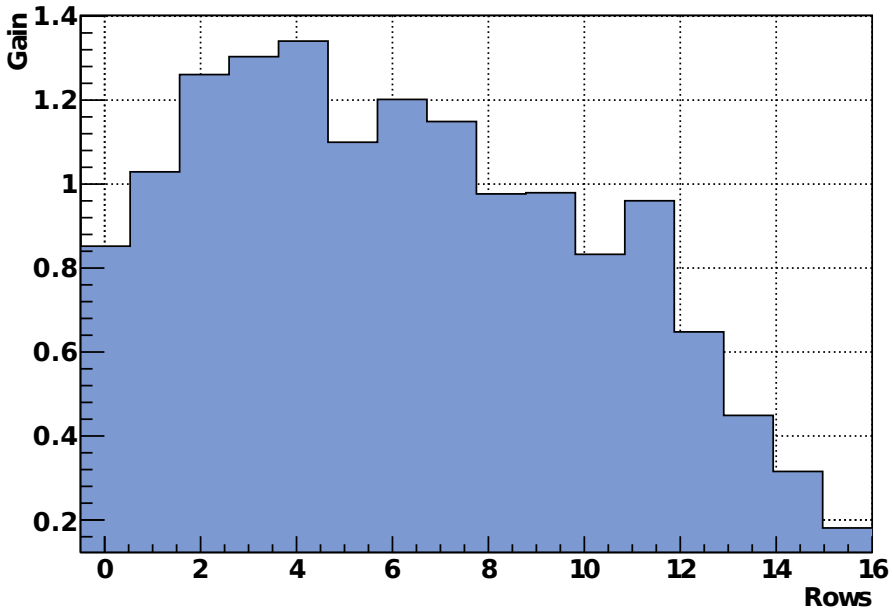

Figure 7.20.: Projection for chamber # 55 (Sector 1, Stack 4, Layer 1).

8. High Voltage Setting

In this chapter the gain dependency of the TRD chambers on the applied high voltage setting is investigated using Krypton data. Two data sets with different high voltage settings were recorded. A total of 130 runs corresponding to $\approx 2 \cdot 10^9$ ^{83}Kr decays for a high voltage setting of 1450V and a total of 51 runs corresponding to $\approx 0.8 \cdot 10^9$ ^{83}Kr decays for a high voltage setting of 1470V were recorded. The data was analyzed using the same analysis procedure described in chapter 7.
The results of the data sets are compared in section 8.1 and the gain variation when increasing the anode high voltage is determined for each chamber. The gain variation results determined within this thesis are compared to previous studies in section 8.2.

8.1. Gain dependency on the applied high voltage

The gain of the TRD chambers depends on the applied anode voltage. The anode voltage directly influences the amplification of the number of electrons in the avalanche, thus the gas gain.

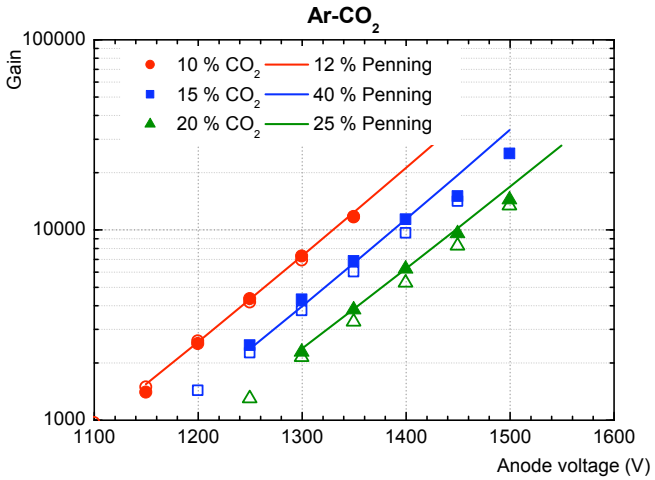

Figure 8.1.: Simulation of gain dependency on the applied anode high voltage of TRD chambers [50].

From electrostatic calculations, it is expected that the gain increases with the anode voltage [35]. Figure 8.1 shows a simulation of the gain dependency on the applied anode high voltage for Ar/CO_2 gas mixture, which consists with these calculations. The recorded data sets with different high voltage settings were analyzed as described in chapter 7 and the mean values of the Gaussian fit are compared.

Figure 8.2 shows the ^{83}Kr decay energy spectrum for one TRD chamber (Sector 8, Stack 0, Layer 1) for two different high voltage settings after applying the same analysis procedure described in chapter 7. The mean value of the peak corresponding to the ^{83}Kr most prominent decay level is respectively (2292.8 ± 0.14) ADC counts for 1450V and (2836.4± 0.2) ADC counts for 1470V. On the other hand the sigma value of this peak is (176.5 ± 0.2) ADC counts for 1450V and (212.4 ± 0.4) ADC counts for 1470V.

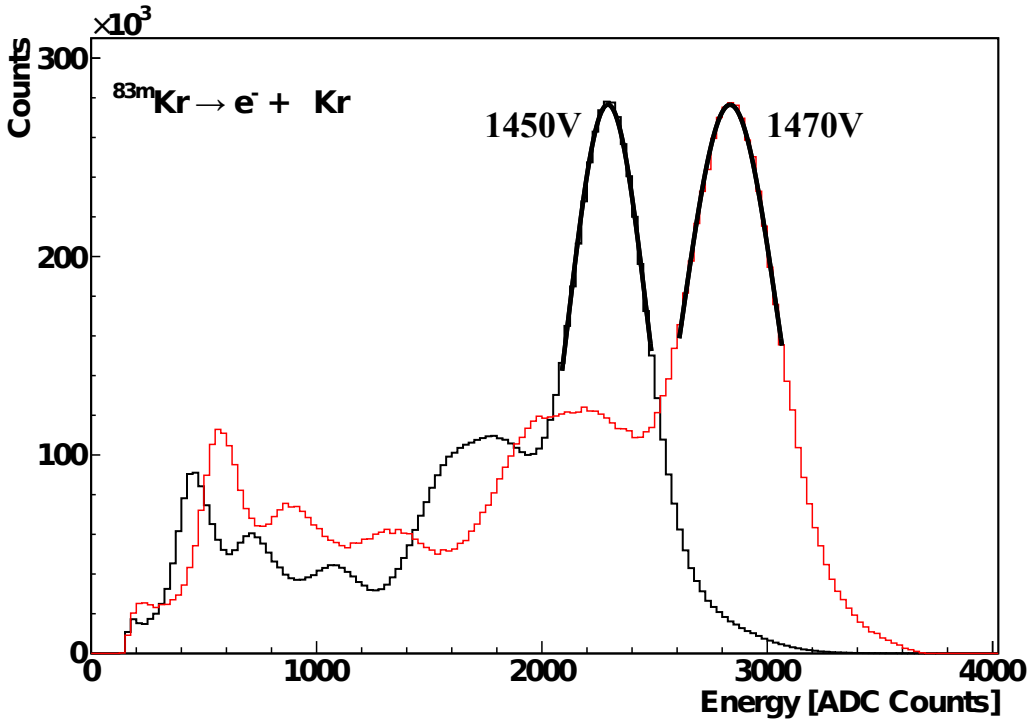

Figure 8.2.: ^{83}Kr decay energy spectrum for one TRD chamber (Sector 8, Stack 0, Layer 1) for the high voltage settings of 1450V and 1470V. The spectrum for the high voltage setting of 1470V is scaled by a factor of 2.5.

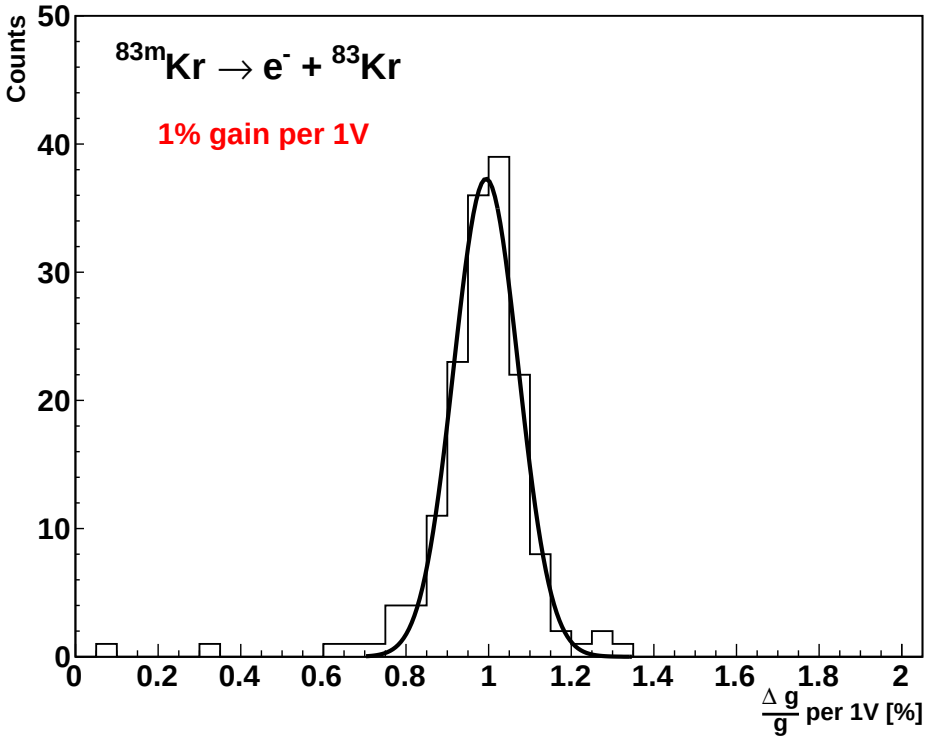

Figure 8.3.: Gain Variation of all chambers in % when increasing the anode high voltage by 1V .

Figure 8.3 shows the relative gain variation of all TRD chambers in percent when increasing the anode high voltage by 1V. The percentage is calculated using the following equation:

$$\text{Gain variation per 1V} = \frac{\Delta\text{gain} \;/\; \text{gain(HV} = 1450\text{V)}}{1470\text{V} - 1450\text{V}} \times 100\ [\%] \qquad (8.1)$$

where $\Delta\text{gain} = \text{gain(HV} = 1470\text{V)} \;-\; \text{gain(HV} = 1450\text{V)}$

The mean value of the Gaussian fit is $(0.994 \pm\ 0.007)\%$. This means that the gain of the TRD chambers increases by $\approx 1\%$ while increasing the anode high voltage by 1V. The tail in this distribution at lower values is due to chambers that had a lower high voltage setting during the calibration run.

The analysis described in this chapter is used to determine individual anode voltages to set constant gain for all TRD installed chambers. A table with factors for each chamber is added to the appendix.

8.2. Comparison to previous studies

In this section the determined gain dependence on the applied high voltage setting using ^{83}Kr is compared to several previous measurements.

In the year 2001, it was done by electrostatic calculations in the *Technical Design Report* of the ALICE experiment [35]. In 2005, S. Freuen investigated the gain of single TRD chambers for his diploma thesis [52], and in 2008, P. Reichelt investigated the same subject for his bachelor thesis [53], [54]. In both theses, radioactive sources were used, and the gain was determined by measuring the current at the anode wires. In 2009, the PhD thesis of R. Bailhache [55] described measurements with cosmic rays in the ALICE pit and recently the diploma thesis of B. Albrecht measurement with cosmic rays in Münster [56]. The measurements are summarized in table 8.1.

Work	Year	Voltage Range (V)	Gas Mixture (%)	Measure
M. Al Helwi	2010	1450-1470	Ar/CO_2(85/15)	Energy deposit
B.Albrecht	2009	1400-1500	Ar/CO_2(83/17	Energy deposit
R.Bailhache	2009	1420-1600	Ar/CO_2(63/37)	Energy deposit
P.Reichelt	2008	1450-1600	Ar/CO_2(70/30)	Anode current
S. Freuen	2005	1350-1500	Ar/CO_2(85/15)	Anode current
Technical report	2001	1350-1500	Xe/CO_2(85/15)	Electrostatic calculations

Table 8.1.: Several measurements of gain in dependence of anode voltage for ALICE TRD chambers [35],[52]-[56].

The measurements used different methods and therefore gave different units of the gain. When the anode wire current is measured, the absolute gain is determined. Relative gain calibrations give gain factors ≈ 1. In order to compare the results, the values for the gain were normalized to give 1.0 for an anode voltage of $1500V$.

According to the calculations in section 8.1, for each measurement the percentage variation in gain for an increase of $1V$ in anode voltage has been calculated with the fit function. Figure 8.4 presents the results, errors were calculated from errors and covariances computed for the fit functions.
The calculation of the relative change in gain for the measurement of S. Freuen [52] gives a relatively large error of $\pm$ 4.3. This is due to the fact that quite large errors are given for the data points of this measurement.
In the range of their accuracy, the calculated gain variations are all of the same size.

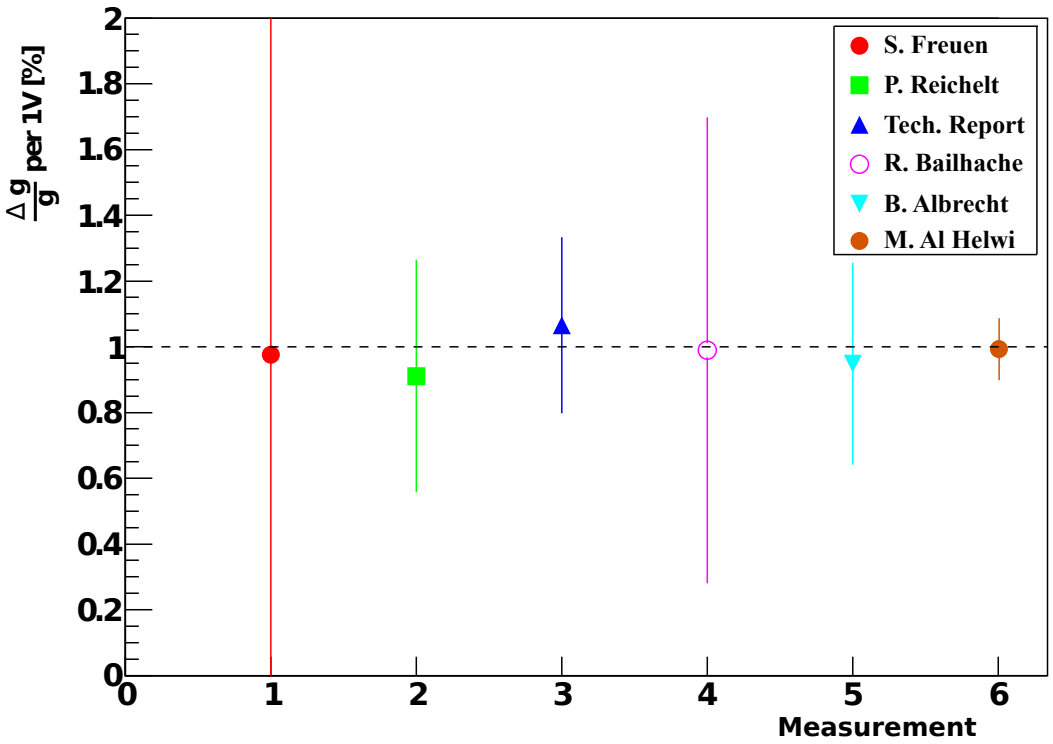

Figure 8.4.: Percentage increase of gain for an increase of $1V$ in anode voltage, calculated with the fit functions to the measurements.

The determined data point within this thesis has the nearest value to the theoretical value, 1% per 1V, and the smallest relative uncertainty. Furthermore figure 8.4 shows the accurateness of the analysis method and developed software used in this thesis, since all compared publications determined the gain variations in different ways.

9. Summary and Outlook

Within this thesis the gain parameters for the ALICE Transition Radiation Detector have been extracted from a dedicated calibration run with a ^{83}Kr source. The radioactive ^{m83}Kr, which was homogeneously distributed in the TRD volume by the gas circulation system, releases electrons with energies between 9 keV and 42 keV. In total $2.8 \cdot 10^9$ Krypton decays in 181 runs were recorded and analyzed.
A detailed Monte Carlo (MC) simulation was performed in order to investigate the induced signal. In contrast to MC-simulations, real data contains a large fraction of noise. Therefore a noise run was recorded and analysed in order to understand its behavior. Cuts for noise reduction were investigated, optimized and implemented.
A complete analysis method for the TRD gain calibration using ^{83}Kr was performed. This method consists of an especially developed analysis software, two scripts and five macros based on the AliRoot framework. This method allows a gain calibration at the finest granularity of the TRD detector, i.e. pad by pad.
A total data size of 30TB were reconstructed using the TRD standard cluster finder. With the developed analysis algorithm, ^{83}Kr clusters were built and the ^{83}Kr decay energy spectrum were filled for a given calibration group, (e.g. chamber, pad) . The peak corresponding to the most prominent ^{83}Kr decay channel of E_{kin} = 41.6keV was fitted with a Gaussian function. The gain was extrapolated from the mean value of the Gaussian fit. The gain fluctuates within 12.7% and the resolution within 5.3% which is consistent with the TRD design specification [35].
The gain parameters for all pads are added to the detector data base in a defined format to be used for offline tracking and to be uploaded to the detector readout front-end-electronics. Furthermore the gain is correlated to the anode voltage applied to the readout chambers. This voltage dependence was investigated using Krypton data with different high voltage settings, and the relative increase in gain given by an increase of 1V in anode voltage has been determined to be about 1%. This result provides the today smallest uncertainties and is in good agreement with the existing measurements and realistic calculations with Magbolz and Garfield.
The developed software package provides an automatic analysis procedure that can be easily applied to further gain calibration measurements using Krypton, e.g. after installing the remaining TRD super-modules. A Consistency check would be a re-production of the Krypton data with applied gain corrections and subsequent fit of the resulting spectrum with negligible residuals.

Appendix A.

Acronyms and Technical Terms

ALICE:	**A** **L**arge **I**on **C**ollider **E**xperiment
ADC:	**A**nalog-to-**D**igital **C**onverter
DAQ:	**D**ata **Aq**uisition
DCS:	**D**etector **C**ontrol **S**ystem
ECS:	**E**xperiment **C**ontrol **S**ystem
FEE:	**F**ront-**E**nd **E**lectronics
FSM:	**F**inite-**S**tate **M**achine
GTU:	**G**lobal **T**racking **U**nit
HLT:	**H**igh **L**evel **T**rigger
HMPID:	**H**igh **M**omentum **P**article **I**dentification
ITS:	**I**nner **T**racking **S**ystem
LHC:	**L**arge **H**adron **C**ollider
MCM:	**M**ulti **C**hip **M**odule
QGP:	**Q**uark **G**luon **P**lasma
RAM:	**R**andom-**A**ccess **M**emory
ROB:	**R**ead**o**ut-**B**oard
SM:	**S**uper**m**odule
TOF:	**T**ime **o**f **F**light
TPC:	**T**ime **P**rojection **C**hamber
TRAP:	**Tra**cklet **P**rocessor
TRG:	Trigger System
TRD:	**T**ransition **R**adiation **D**etector

Appendix B.

Gain dependency on the applied anode high voltage setting

Chamber #	Mean(HV=1450V)	Mean(HV=1470V)	$\frac{\Delta g}{g}$per1V[%]
0	2426.66±0.164011	2915.83±0.516281	1.0079±0.516203
1	2425.64±0.144748	2925.38±0.494092	1.0301±0.494019
2	1758.66±0.0572022	2061.7±0.239665	0.861551±0.239585
3	2581.39±0.566893	3096.54±2.30543	0.997806±2.30537
4	2383.16±0.388628	2815.76±0.87332	0.907614±0.87321
5	2239.45±0.433482	2630.76±2.58526	0.873655±2.58522
6	2176.22±0.103483	2605.23±0.351681	0.985689±0.3516
7	2341.26±0.147084	2835.71±0.506357	1.05595±0.506282
8	2748.62±0.596272	3340.15±2.4531	1.07604±2.45305
9	2663.46±1.01539	3152.93±3.23512	0.918869±3.23505
10	2620.13±0.212491	3146±0.567717	1.00353±0.567631
11	2865.47±3.01713	3406.12±16.5383	0.943385±16.5382
12	2588.68±0.215247	3134±0.777006	1.05328±0.776941
13	2273.25±0.206407	2742.92±0.727132	1.03305±0.727056
14	2792.7±0.224121	3375.51±0.848108	1.04344±0.848051
15	245.586±0.0267805	276.075±0.0661681	0.620738±0.0652352
16	2698.51±0.310257	3262.73±0.94017	1.04542±0.940096
17	2257.23±0.212262	2672.83±0.813892	0.920599±0.813824
18	2477.55±0.115048	3007.33±0.357615	1.06916±0.357536
19	2325.89±0.184107	2812.34±0.607319	1.04571±0.607241
20	2543.17±0.183411	3067.95±0.615635	1.03173±0.615564
21	2030.87±0.216399	2389.64±0.834146	0.883287±0.83407
22	2217.15±0.139743	2657.15±0.626772	0.992282±0.626712
23	2502.95±0.356962	2989.65±1.50185	0.972259±1.50179
24	2894.24±1.3041	3495.61±5.5168	1.03892±5.51675
25	2307.12±0.125841	2779.31±0.452658	1.02333±0.452585
26	2467.35±1.42776	2990.27±5.85236	1.05968±5.8523
27	2221.32±0.152292	2642.04±0.499349	0.947015±0.499267
28	2136.45±0.678415	2168.45±2.22258	0.074889±2.2225
29	2170.69±0.149747	2578.51±0.384148	0.939377±0.384041

Table B.1.: Gain dependency on the applied high voltage for the installed chambers of TRD Sector 1

Chamber #	Mean(HV=1450V)	Mean(HV=1470V)	$\frac{\Delta g}{g}$per1V[%]
30	1103.24±0.258839	1180.44±0.152729	0.349877±0.151904
31	2298.5±0.365748	2746.6±1.2597	0.974785±1.25963
33	2093.63±0.40015	2454.28±1.64352	0.861294±1.64345
34	2764.29±0.275108	3308.72±0.849947	0.984768±0.849877
35	2274.53±0.379649	2616.62±1.48294	0.75201±1.48287
36	2503.3±0.256939	3017.03±0.856414	1.02611±0.856342
37	2345.65±0.217813	2854±0.77546	1.08361±0.775387
38	2318.52±0.20051	2797.57±0.663826	1.03308±0.663748
39	2461.94±0.253618	2965.26±0.909832	1.02218±0.909764
40	2865.56±0.407297	3392.59±1.65393	0.919596±1.65388
41	2266.26±0.158335	2701.45±0.577756	0.960156±0.577684
42	2595.03±0.303951	3138.46±1.02757	1.04707±1.0275
43	2469.83±0.245863	2982.75±0.892681	1.03836±0.892614
44	2550.78±0.163648	3074.36±0.622977	1.02632±0.622915
45	2546.42±0.245215	3074.15±1.00766	1.03622±1.0076
46	2530.03±0.177438	3005.54±0.649811	0.939731±0.649747
47	2818.04±0.531911	3384.31±1.98595	1.00473±1.98589
48	2665.75±0.677056	3225.12±2.07502	1.04918±2.07495
49	2568.16±0.753466	3123.14±2.43236	1.08051±2.43229
50	2753.38±0.405334	3310.12±1.41069	1.01102±1.41062
51	2246.04±0.429393	2670.29±1.74201	0.944441±1.74195
54	2502.45±0.273076	3008.77±0.830313	1.01165±0.830234
55	2639.84±0.990974	3154.19±2.97561	0.974205±2.97553
56	2697.99±1.29087	3280.45±3.65362	1.07944±3.65354
57	2767.21±0.362377	3307.89±1.34643	0.976938±1.34638
58	2565.45±0.358348	3061.05±0.87487	0.965906±0.874775

Table B.2.: Gain dependency on the applied high voltage for the installed chambers of TRD Sector 2

Chamber #	Mean(HV=1450V)	Mean(HV=1470V)	$\frac{\Delta g}{g}$per1V[%]
210	2460.37±0.133382	2939.92±0.382205	0.974564±0.38212
211	2787.11±1.7151	3406.85±7.10527	1.11179±7.10522
212	1896.38±0.225166	2259.07±1.37501	0.956257±1.37496
213	1940.89±0.218779	2332.5±0.957094	1.00883±0.957023
214	2539±0.14814	3029.89±0.411037	0.966692±0.410952
215	2633.66±0.639951	3190.12±1.59326	1.05644±1.59317
216	2521.54±0.168825	3047.97±0.487883	1.04388±0.4878
217	2621.72±0.276832	3189±0.876147	1.08187±0.876073
218	2485.27±0.156077	3004.32±0.552504	1.04425±0.552435
219	2080.06±0.178723	2492.59±0.620061	0.991621±0.619978
220	2178.51±0.0872029	2604.68±0.363896	0.978121±0.363831
221	2648.8±0.232544	3188.63±0.760478	1.01901±0.760409
222	2500.3±0.276977	3016.72±0.890943	1.03272±0.890868
223	2859.53±0.389089	3461.97±1.51898	1.05338±1.51893
224	2958.12±0.737441	3551.87±3.62408	1.00359±3.62404
225	2765.08±0.493935	3323.59±1.5932	1.00993±1.59313
226	2771.18±0.916837	3291.27±2.87849	0.938387±2.87842
227	2368.79±0.215582	2813.9±0.72755	0.939535±0.727476
229	2607.74±0.168744	3125.54±0.593918	0.992805±0.593852
230	2806.06±0.878335	3365.33±2.11057	0.996552±2.11048
231	2350.05±0.188119	2809.97±0.694778	0.978517±0.69471
232	2294.13±0.120327	2739.55±0.506913	0.970776±0.506851
233	2602.28±0.407314	3076.16±1.69147	0.910516±1.69141
234	2580.58±0.411726	3059.72±1.18983	0.928362±1.18975
235	2255.71±0.118601	2682.74±0.418911	0.946567±0.418837
237	1650.01±0.332668	1891.38±1.13549	0.731439±1.13539
238	2371.93±0.131406	2812.19±0.447033	0.928045±0.446959
239	2551.14±0.172844	3028.75±0.591858	0.936076±0.59179

Table B.3.: Gain dependency on the applied high voltage for the installed chambers of TRD Sector 7

Chamber #	Mean(HV=1450V)	Mean(HV=1470V)	$\frac{\Delta g}{g}$per1V[%]
240	2196.34±0.169588	2660.48±0.541869	1.05661±0.541782
241	2292.91±0.14682	2804.39±0.543576	1.11534±0.543504
242	2348.57±1.9908	2752.35±1.16694	0.859623±1.16652
243	2333.62±1.60325	2731.18±0.977567	0.85183±0.977156
244	2287.83±0.099933	2866.14±0.313427	1.26388±0.31334
245	2354.36±0.404501	2909.87±1.53337	1.17975±1.5333
246	2158.46±0.101363	2650.35±0.347227	1.13945±0.347144
247	2043.22±0.157151	2487.61±0.566515	1.08745±0.566433
248	2278.99±1.1355	2665.25±0.770525	0.847445±0.770147
249	2558.09±1.6794	3013.74±1.05826	0.89062±1.0579
250	2567.96±0.21408	3232.56±1.07762	1.29404±1.07757
251	2358.49±0.183325	2901.19±0.645348	1.15052±0.645274
252	2323.04±0.16935	2844.22±0.550807	1.12176±0.550726
253	2386.19±0.317828	2912.32±1.06679	1.10245±1.06671
254	2662.72±3.06133	3144.77±2.34281	0.905176±2.34252
255	1933.17±3.25091	2246.67±2.15921	0.810842±2.15876
256	2383.74±0.177426	2969.57±0.751183	1.22882±0.751122
257	2389.74±0.306313	2927.3±1.02518	1.12473±1.02511
258	2091.49±0.0858326	2555.2±0.268275	1.10856±0.268181
259	2249.32±0.244282	2731.24±0.936123	1.07126±0.936052
261	2409.28±1.02749	2824.2±0.651469	0.861074±0.651085
262	2083.62±0.381583	2531.18±1.8192	1.07401±1.81914
263	2888.8±0.400092	3520.9±1.99929	1.09406±1.99925
264	2298.01±0.192509	2789.16±0.562214	1.06864±0.562124
265	2259.02±0.441292	2736.42±1.48887	1.05664±1.48879
266	2413.74±0.887296	2799.93±0.551045	0.799983±0.550658
267	2597.31±2.06905	3039.23±1.19282	0.850736±1.19243
268	2018.25±0.180386	2543.2±0.61221	1.3005±0.612118
269	2576.28±0.236825	3158.94±0.762707	1.13082±0.762634

Table B.4.: Gain dependency on the applied high voltage for the installed chambers of TRD Sector 8

Chamber #	Mean(HV=1450V)	Mean(HV=1470V)	$\frac{\Delta g}{g}$per1V[%]
270	2372.35±0.182042	2836.28±0.665919	0.977786±0.66585
271	2247.74±0.114629	2688.83±0.468064	0.981187±0.467999
272	2625.02±0.52075	3155.84±1.788	1.01107±1.78793
274	2589.22±0.198026	3086.08±0.699919	0.959464±0.699854
275	1849.87±0.367984	2102.01±1.02706	0.681506±1.02695
276	2909.04±0.786823	3521.12±2.58504	1.05203±2.58497
277	2365.01±0.124428	2843.54±0.624155	1.0117±0.624105
278	3574.35±11.1903	4130.52±27.2644	0.778006±27.2643
279	2091.73±0.178066	2472.47±0.610918	0.910109±0.610836
282	2411.62±0.293484	2929.17±0.946028	1.07302±0.945949
283	2478.04±0.202262	2970.26±0.715197	0.993177±0.715128
284	2531.38±0.31213	3058.17±1.15688	1.04052±1.15682
285	2000.53±0.273392	2393.61±1.31904	0.982438±1.31898
286	2600.88±0.290112	3123.34±0.96201	1.00438±0.96194
287	2481.38±0.248186	2967.39±0.942813	0.979313±0.94275
288	2153.05±0.127852	2585.39±0.489629	1.00402±0.489557
289	2500.44±0.252468	3024.56±0.718055	1.04805±0.71797
290	2057.63±0.873325	2499.45±2.66648	1.07359±2.66638
291	1894.87±0.305186	2287.88±1.40414	1.03704±1.40407
292	2541.63±0.293761	3055.74±0.868217	1.01137±0.868137
294	2498.72±0.200419	2962.68±0.647811	0.928397±0.647738
295	2251.02±0.187598	2693.64±0.861267	0.983156±0.861209
296	2505.54±0.174369	2984.23±0.581289	0.955256±0.581217
297	2549.79±0.328723	3012.36±1.19204	0.907074±1.19197
298	2057.52±0.181226	2435.73±0.921392	0.919069±0.921336
299	2372.76±0.388182	2770.1±2.96188	0.837307±2.96185

Table B.5.: Gain dependency on the applied high voltage for the installed chambers of TRD Sector 9

Chamber #	Mean(HV=1450V)	Mean(HV=1470V)	$\frac{\Delta g}{g}$per1V[%]
300	2228.14±0.110478	2681.39±0.358851	1.01712±0.358768
301	2705.86±1.10105	3304.59±4.03065	1.10636±4.03059
302	2466.74±0.152385	2966.02±0.493038	1.01202±0.492963
303	2393.1±0.212244	2922.56±0.746771	1.10621±0.746699
304	2460.68±0.134369	2969.65±0.478171	1.03421±0.478103
305	2956.29±1.34862	3532.57±9.5004	0.974679±9.50038
306	2386.93±0.132814	2903.54±0.497392	1.08215±0.497324
307	2611.72±3.41677	3212.49±8.69749	1.15015±8.6974
308	2626.93±1.02599	3183.2±3.91197	1.05879±3.91191
309	2441.94±0.241831	2965.49±0.801439	1.07199±0.801364
310	2647.4±0.184078	3210.68±0.52848	1.06383±0.5284
311	2432.14±0.244322	2912.2±0.767233	0.986903±0.767154
312	2473.42±0.158094	3012.03±0.521813	1.0888±0.521738
313	2284.1±0.154882	2774.87±0.527836	1.07431±0.527758
314	2346.15±0.134563	2850.68±0.466973	1.07524±0.466898
315	2072.3±0.247008	2522.3±0.977923	1.08575±0.977849
316	2342.65±0.169573	2828.49±0.682907	1.03694±0.682843
317	2061.66±0.238451	2504.26±0.911421	1.07342±0.911343
318	2553.28±0.181057	3087.42±0.632162	1.04599±0.632094
319	2626.22±0.216325	3216.95±0.691776	1.12468±0.691704
320	2653.44±0.599229	3222.76±1.84491	1.07279±1.84484
321	2641.06±0.272183	3233.4±0.922374	1.1214±0.922306
322	2548.05±0.156223	3101.09±0.458132	1.08522±0.45805
323	2745.76±0.237906	3345.76±0.816071	1.0926±0.816006
324	2400.13±0.193909	2915.7±0.621499	1.07406±0.62142
325	2421.85±0.219624	2949.12±0.694888	1.08857±0.694808
326	2785.96±0.504116	3377.05±2.19731	1.06084±2.19726
327	2402.33±0.155111	2908.01±0.530589	1.05248±0.530516
328	2412.52±0.129715	2936.77±0.440093	1.0865±0.440018
329	2196.89±0.651555	2265.72±1.04566	0.156636±1.04551
510	2494.15±0.160682	2978.49±0.472897	0.970949±0.472816

Table B.6.: Gain dependency on the applied high voltage for the installed chambers of TRD Sector 10

Chamber #	Mean(HV=1450V)	Mean(HV=1470V)	$\frac{\Delta g}{g}$per1V[%]
511	338.517±0.029241	3176.57±3.5281	41.919±3.52799
512	356.564±0.156268	3292.31±11.6206	41.1672±11.6205
513	2001.35±0.398953	2306.21±0.861345	0.761648±0.861212
514	2320.64±0.172347	2792.41±0.805432	1.01646±0.805377
515	2250.05±0.140524	2616.92±0.567978	0.815247±0.567914
516	2532.28±0.174546	3039.52±0.505049	1.00154±0.504967
517	447.075±0.0944099	2452.94±2.11914	22.4332±2.11887
518	2598.1±0.317197	3082.44±1.12045	0.932107±1.12039
519	1895.99±0.213081	2228.42±0.85164	0.876654±0.851562
520	398.564±0.0913921	2321.14±6.02337	24.1188±6.02326
521	2751.82±1.52385	3297.53±5.03451	0.991543±5.03444
522	2497.61±0.180892	2974.46±0.597078	0.954597±0.597006
523	336.52±0.0530582	3073.04±1.22201	40.6591±1.22142
524	472.698±0.117699	3352.26±2.28553	30.4588±2.28515
525	2539.86±0.130623	3034.8±0.435539	0.974337±0.435469
526	512.375±0.0986568	2857.26±1.2393	22.8825±1.23886
527	480.567±0.123006	3467.95±1.31117	31.0818±1.31047
528	2064.65±0.180387	2473.39±1.00255	0.989841±1.0025
529	2262.57±0.122608	2735.89±0.431575	1.04597±0.431499
530	2622.57±0.216297	3146.04±0.757499	0.998019±0.757434
531	2526.72±0.158571	3024.07±0.534143	0.984179±0.534072
532	2707.22±0.330112	3238.01±1.66592	0.980326±1.66587
534	2831.7±1.36134	3432.51±3.93155	1.06086±3.93147
535	2356.68±0.161693	2819.03±0.60131	0.980936±0.601242
536	2480.97±0.467482	2943.09±1.41761	0.931328±1.41753
537	2357.94±0.191156	2777.28±0.863184	0.889218±0.863129
538	263.742±0.0698274	3078.16±4.77355	53.3555±4.77323

Table B.7.: Gain dependency on the applied high voltage for the installed chambers of TRD Sector 17

Bibliography

[1] LHC webpage, http://lhc.web.cern.ch/lhc/.

[2] X. Zhu *et al.*, Phys. Lett. **B647** (2007) 366.

[3] L Yan, P. Zhuang and N. Xu, Phys. Rev. Lett. **97** (2006) 232301.

[4] B. Zhang, L.W. Chen and C-M. Ko, Phys. Rev. **C72** (2005).

[5] P. Braun-Munzinger and J. Stachel, Nucl. Phys. **A690** (2001) 119c.

[6] A. Andronic *et al.*, Phys. Lett. **B571** (2003) 36.

[7] M.C. Abreu *et al.*, Phys. Lett. **B499** (2001) 85.

[8] P. Braun-Munzinger and J. Stachel, Phys. Lett. **B490** (2000) 196.

[9] A. Andronic et al., Phys. Lett. **B652** (2007) 259.

[10] I. Vitev and M. Gyulassi, Phys. Rev. Lett. **89** (2002) 252301.

[11] P. Jacobs and X. Wang, Prog. Part. Nucl. Phys **54** (2005) 443.

[12] R. Vogt, Eur. Phys. **J 155** (2008) 213.

[13] A. Wachter and H. Hoeber, *Repetitorium Theoretische Physik*, (Springer, 2005).

[14] E. Sicking, Diploma Thesis, University of Münster (2009).

[15] B. Povh *et al.*, *Teilchen und Kerne*, (Springer, 2006).

[16] Fermilab, Office of Science, United States Department of Energy.

[17] K. Schweda, and N. Xu, Partonic Collectivity in high-energy nuclear collisions, Acta Phys. Hung. **A22**, 102 (2005).

[18] http://public.gettysburg.edu/ mstrickl/images/.

[19] R. P. Feynman, Proceedings of the 3rd Topical Conference on High Energy Collision of Hadrons, Stony Brook, N. Y. (1969)

[20] K. Yagi *et al.*, *Quark-Gluon Plasma*, (Cambridge Univ. Press, 2004).

[21] F.Karsch, BI-TP 2001/06 (2001).

[22] T. Hatsuda, J. Phys. **G**: Nucl. Part. Phys. 34 (2007) S287.

[23] Y. Aoki *et al.*, Nature 443 (2006) 675.

[24] W. H. Smith, *LHC startup*, arXiv:0808.3131 [hep-ex].

[25] ALICE Collaboration, ALICE: Physics Performance Report, Volume I, J. Phys. **G 30** (2004) 1517.

[26] The Inner Tracking System of the ALICE Experiment at the CERN LHC, CERN-ALI-98-14 ; CERN-ALICE-PUB-98-14.

[27] ALICE Collaboration, ALICE TDR 010, CERN-LHCC-2003-062 (2004).

[28] D. H. Perkins, *Introduction to High Energy Physics*, (University Press, Cambridge, 2000).

[29] P. Giubellino, Heavy Ion Physics at the LHC, arXiv:0809.1062 [nucl-ex] (2008).

[30] ALICE Collaboration, ALICE: Physics Performance Report, Volume II, J. Phys. **G 32** (2006) 1295.

[31] A. Wilk *et al.*, Nucl. Instrum. Meth. **A 563** (2006) 314.

[32] A. Wilk, Diploma Thesis, University of Münster (2004).

[33] W. Sommer, Dissertation, University of Frankfurt (2008).

[34] J. Cuveland, Diploma Thesis, University of Heidelberg, (2003).

[35] ALICE Collaboration, CERN/LHCC2001-021. ALICE - Technical Design Report of the Transition Radiation Detector (2001).

[36] ALICE Collaboration. ALICE - Technical Paper I (2008).

[37] S. Afanasiev *et al.*, Nucl. Instrum. Meth. **A 430** (1999) 210.

[38] B. Lasiuk and C. A. Whitten, "Use of Krypton-83 as a calibration source for the STAR TPC." STAR Note 360, (1998).

[39] J. Thaeder, private communication.

[40] C.Garabatos Cuadrado and D.Vranic, private communication.

[41] F. Sauli, Principle of operation of multiwire propotional and drift chambers, CERN 77-09 (1976).

[42] D. Decamp et al., "ALEPH: A detector for electron–positron annihilations at LEP," Nucl. Instrum. Meth. **A 294** (1990) 121.

[43] A. Chan et al., "Performance of the HPC calorimeter in DELPHI," IEEE Transactions on Nuclear Science, **A 42** (1995) 491.

[44] B. Lasiuk and C. A. Whitten, STAR Note 360, (1998).

[45] ALICE Collaboration, http: // aliceinfo. cern. ch , (2009).

[46] Root - a data analysis framework. http: // root. cern. ch , (2009).

[47] S. Radomski, private communication.

[48] Y. Pachmayer, private communication.

[49] H. Yang, private communication.

[50] A. Andronic *et*, Drift velocity and gain in argon- and xenon-based mixtures.

[51] Particle Data Group, C. Amsler *et al.*, Phys. Lett. **B 667** (2009).

[52] S. Freuen, Diploma Thesis, University of Heidelberg, (2005).

[53] P. Reichelt, Bachelor Thesis, University of Frankfurt, (2008).

[54] M. Appelshäuser *et al*,Measurement of the gas amplification of alice-trd chambers at the ikf. GSI Scientific Report, INSTRUMENT-METHODS-50:270, (2008).

[55] R. Bailhache, Ph.D. Thesis, Darmstadt University of Technology, (2009).

[56] B. Albrecht, Diploma Thesis, University of Münster, (2010).

Acknowledgments

This work would not have been possible without the support of numerous people.
First and foremost I would like to express my gratitude to my supervisor Dr. Kai Schweda for providing me this interesting topic. During this year I profited very much from his enthusiasm, knowledge and advice. He was always interested in the current status of my work and gave me the vital encouragement and support. Furthermore I would like to thank Professor Dr. Johanna Stachel for making it possible for me to work in her team and for giving me the possibility to take part in a unique experiment.
I'm thankful that Professor Dr. Dirk Dubbers agreed to be the second corrector of this thesis.
Many thanks go to Dr. Yvonne Pachmayer and Dr. Jens Wiechula for their constant support throughout the year, for the possibility to pass on knowledge to new students.
Furthermore, from the University of Heidelberg, I would like to thank: Katrin Koch, Sara Vallero and Jochen Klein for helping with AliRoot questions, and Dr. Hongyan Yang for her diverses helps especially with the understanding of noise.
From GSI I would like to thank:
Dr. Silvia Masciocchi, Markus Fasel and Dr. Kilian Schwarzer for helping by copying the data sets to GSI, Dr. Anton Andronic and Dr. Marian Ivanov for many discussions concerning the calibration, and Dr. Dariusz Miskowiec for organizing the analysis/calibration/alignment meeting.
I would also like to thank the people I mainly know from CERN, especially:
Dr. Chilo Garabatos for many helps concerning the gas system and the source installation, Dr Latchezar Betev for taking care of the reconstruction done at CERN.
Last, but certainly not least, I thank the most important people in my life, my family. All of this would not have been possible without their unconditional support.

This work has been supported by the Helmholtz Association under contract number VH-NG-147 and the German Federal Ministry of Education and Research under promotional reference 06HD197D.

Erklärung

Ich versichere, dass ich diese Arbeit selbständig verfasst und keine anderen als die angegebenen Quellen und Hilfsmittel benutzt habe.

Heidelberg, den 31.05.2010 .....

Mustapha Al Helwi